Mesoscale modulation of marine boundary layer water vapor isotopologues during ~~EUREC4A~~EUREC^{4}A

Joseph Galewsky[1] and Sebastian A. Los[1]

[1]Department of Earth and Planetary Sciences, University of New Mexico, Albuquerque, New Mexico, United States

Correspondence: Joseph Galewsky (galewsky@unm.edu)

Abstract. Shallow cumulus clouds in trade-wind regions remain ~~a major~~ an important source of uncertainty in climate projections, with ~~conflicting hypotheses about~~ competing interpretations of how mesoscale circulations ~~affect~~ influence boundary layer moisture. We analyze water vapor isotopologue measurements from the EUREC^{4}A campaign to quantify the mesoscale modulation of marine boundary layer humidity and isotopic composition. Surface ~~δD~~ δD measurements from R/V ~~Meteor show remarkably~~ *Meteor* show a strong sensitivity to mesoscale vertical ~~motions, responding 7.5 times more strongly than humiditywhen normalized by observed standard deviations. Mesoscale upward motion counteracts~~ velocity relative to humidity. Regression analyses show that mesoscale ascent partially offsets entrainment-driven isotopic depletion~~with an efficiency of 1.19, meaning 1 mm~~: approximately 0.7 mm s^{-1} of ~~vertical velocity more than cancels~~ upward motion is required to counteract the isotopic effect of 1~~mm~~ mm s^{-1} of entrainment. The strongest correlations between vertical velocity and both ~~δD~~ δD ($r \approx 0.52$) and mixing ratio ($r \approx 0.39$) occur within ±200 m of the subcloud layer ~~(SCL)~~ top. A steady-state flux-form mixed-layer model ~~reproduces these asymmetric responses, providing mechanistic understanding of how mesoscale circulations fundamentally modulate boundary layer moisture processes~~shows that modest below-cloud rain evaporation can reproduce the observed asymmetric response by adding both vapor mass and isotopic mass with an isotopic composition distinct from the ambient subcloud layer. In the model, an ascent-dependent drizzle source rotates the fitted δD contours relative to humidity, whereas a no-rain control collapses this separation. These results support below-cloud rain evaporation as a physically consistent mechanism through which mesoscale circulations can reorganize moisture pathways without producing commensurate changes in total water vapor.

1 Introduction

Shallow cumulus clouds in the trade-wind regions are ubiquitous and exert a cooling influence on the climate, but their response to warming remains ~~highly~~ uncertain (Bony and Dufresne, 2005). These low clouds have long been recognized as a leading source of spread in climate model projections of global warming (Sherwood et al., 2014). Many climate models predict a positive trade cumulus cloud feedback governed by reductions in cloud fraction near cloud base. In particular, higher-sensitivity models tend to produce more efficient entrainment of dry air from aloft, which depletes low-level humidity and erodes cloud cover (Sherwood et al., 2014). This hypothesized mixing–desiccation mechanism posits that vigorous shallow convective mixing dries the lower troposphere and dissipates clouds, thereby amplifying surface warming as a positive low-cloud feedback.

Recent observations, however, challenge this ~~simple~~ picture. In early 2020, the EUREC^{4}A field campaign (Elucidating the Role of Clouds–Circulation Coupling in Climate) was conducted near Barbados with a ~~comprehensive~~ network of research aircraft, ships, and ground stations to study trade-wind cumulus and their environment (Bony et al., 2017; Stevens et al., 2021). Analyses of EUREC^{4}A data revealed ~~ubiquitous~~ shallow mesoscale circulations on scales of roughly 100–200 km that organize convection and concentrate moisture in the trades (George et al., 2023). Consistent with this, periods of stronger mesoscale ascent did not lead to a drier subcloud layer (SCL) or reduced cloudiness, contrary to the mixing–desiccation expectation (Vogel et al., 2022). Instead, the observations suggest that mesoscale cloud–circulation coupling can maintain humidity, implying that factors beyond one-dimensional entrainment, such as horizontal convergence and large-scale vertical motion, significantly influence ~~low-level~~ low-level moisture and cloud cover. Nevertheless, disentangling the contributions of these processes, for example separating the effects of shallow convective detrainment from those of large-scale subsidence, remains challenging with conventional measurements alone. Standard thermodynamic observations cannot easily attribute moisture variability to specific physical processes, leaving an important gap in process-level understanding of the trade cumulus regime.

Stable water isotopologues offer a way to fill this gap. The ratios of heavy to light water isotopologues in vapor, such as $H_2^{18}O/H_2^{16}O$ or HDO/H_2O, commonly reported as δ^{18}O and ~~δD~~ δD, are sensitive to the cumulative phase-change history of an air mass (Galewsky et al., 2016). Condensation and rainout preferentially remove heavy isotopes, so air that has undergone extensive convective uplift and precipitation is left isotopically depleted in heavy molecules relative to ocean water. In contrast, ~~addition of moisture by evaporation from the warm ocean surface, or by mixing with unsaturated air from below, enriches the vapor in heavy isotopes~~vapor added by ocean evaporation is comparatively enriched, and below-cloud evaporation of falling hydrometeors can return isotopically distinct condensate-derived water to the subcloud layer (Tremoy et al., 2014; Graf et al., 2019). Thus, water vapor isotopic measurements can serve as tracers of moisture origin and transport. They enable us to distinguish ~~between air masses that have experienced different water-cycle processes and to test hypotheses about what controls an air mass's humidity and cloud-forming potential~~among surface evaporation, entrainment, and rain-evaporation contributions that may have similar effects on total humidity but different effects on isotopic composition. Past studies have demonstrated that isotopic variations can be used to identify moisture sources and quantify mixing between atmospheric layers, processes that are largely indistinguishable in bulk humidity alone ~~(Risi et al., 2019; Galewsky et al., 2016)~~(Risi et al., 2020; Galewsky et al., 2016).

~~Motivated by this,~~ EUREC^{4}A included a coordinated initiative (EUREC^{4}A-iso) to deploy an extensive network of water vapor isotope analyzers across multiple platforms (Bailey et al., 2023). Seven laser-based instruments, sampling at up to 0.5 Hz, were operated on two research aircraft, three ships, and at the Barbados Cloud Observatory during the campaign. This data set provides the high-resolution, multi-platform coverage needed to close regional moisture budgets and ~~rigorously~~ evaluate model simulations of moist processes. Here, we ~~leverage~~ use the EUREC^{4}A water vapor isotopic measurements from the R/V Meteor to bridge the gap between documented mesoscale circulation effects and their impacts on the marine boundary layer moisture budget. Specifically, we use the stable isotope signatures to ~~directly track shallow convective mixing and its influence on~~ test how entrainment, mesoscale ascent, and below-cloud rain evaporation jointly shape lower-tropospheric moisture in the trade-wind regime.

2 Data

~~EUREC4A comprised roughly~~ EUREC^{4}A comprised about 5 weeks of measurements in the downstream winter trades of the North Atlantic, eastward and southeastward of Barbados. The campaign deployed an extensive observational network to characterize processes operating across scales from micrometers to hundreds of kilometers. The measurements included 2500 atmospheric soundings to quantify mesoscale and larger-scale ~~circulations~~atmospheric properties, approximately 400 flight hours by four research aircraft, operations from four research vessels, and continuous observations from a ground-based cloud observatory. Additional platforms included autonomous systems that collected nearly 10,000 upper-ocean profiles, continuous atmospheric boundary layer measurements, air-sea interface observations, water vapor isotopologue measurements across multiple platforms, coordinated satellite observations, and support from high-resolution numerical weather and climate models.

2.1 Upper Air Data

The dropsonde measurements were conducted using two research aircraft: the High Altitude and Long Range Research Aircraft (HALO) ~~dropsonde measurements were conducted as a core part of the EUREC4A field campaign~~(Konow et al., 2021) and the NOAA WP-3D Orion (P-3) (Pincus et al., 2021). The primary scientific motivation for these measurements was to characterize the ~~mesoscale meteorological~~ area-averaged kinematic environment of trade-wind cumulus cloud fields and to quantify area-averaged vertical motion in the marine boundary layer. The cornerstone of the ~~HALO~~ measurement strategy was the ~~EUREC4A-circle~~ EUREC^{4}A-circle (Figure 1), a standardized circular flight pattern designed to enable accurate estimates of ~~mesoscale circulation~~ properties including divergence, vorticity, and vertical velocity. This approach, adapted from Lenschow et al. (1999, 2007) and Bony and Stevens (2019), exploits the assumption that atmospheric variations at the mesoscale can be approximated as linear in horizontal space over the scale of a single aircraft circle.

The ~~EUREC4A-circle~~ EUREC^{4}A-circle was centered at 13.30°N, 57.72°W with a diameter of approximately 222 km. Each circle flight pattern deployed 12 dropsondes at regular intervals around the circumference, with launches separated by approximately 5 minutes corresponding to the aircraft's 60-minute circuit time. This systematic sampling enables estimation of horizontal gradients through regression analysis, from which mesoscale circulation properties can be derived.

A total of ~~70 EUREC4A-circles were flown by HALO~~ 85 EUREC^{4}A-circles were flown during the campaign (71 by HALO and 14 by the P-3), providing unbiased sampling across meteorological conditions. ~~HALO~~ All flights operated from Bridgetown, Barbados, with HALO operating at altitudes between 10.0–10.5 km, while the P-3 typically flew at lower altitudes near 7.5 km as part of the ATOMIC component of the campaign (Pincus et al., 2021). A total of ~~895~~ 1215 Vaisala RD-41 dropsondes were launched (895 from HALO and 320 from the P-3), each containing pressure, temperature, and humidity sensors sampling at 2 Hz, along with GPS receivers providing wind measurements at 4 Hz. The measurements are archived in the JOANNE dataset (George et al., 2021), from which we use the Level 4 circle-averaged products containing mesoscale diagnostics derived through regression analysis of the 12-sonde circle patterns. These products include horizontal gradients of

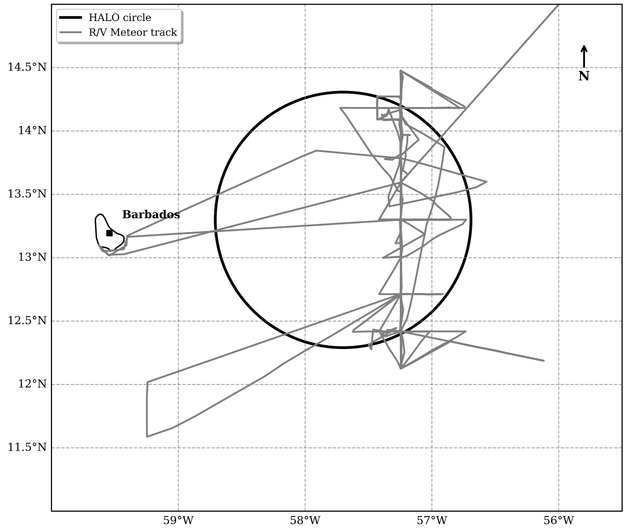

Figure 1. Map of the ~~EUREC4A~~ EUREC^{4}A study area showing a representative ~~HALO~~ EUREC^{4}A circle pattern and the R/V Meteor ship track. The circle (black) represents one of the 222 km diameter flight patterns used for dropsonde deployment to measure mesoscale circulation. The ship track (gray) shows the path of R/V Meteor during the January–February 2020 field campaign.

atmospheric variables and derived quantities such as divergence, vorticity, horizontal divergence of wind velocity, and vertical velocity, with associated uncertainty estimates from the regression fitting.

The subcloud layer height h used here was first presented in Vogel et al. (2022) and is determined using a temperature-based threshold method (Albright et al., 2022). Specifically, h is defined as the height where the virtual potential temperature θ_v first exceeds its density-weighted mean value (computed from 100 m up to h) by a fixed threshold $\epsilon = 0.2$ K (Vogel et al., 2022). This approach follows established methodology for identifying the top of the well-mixed subcloud layer (Touzé-Peiffer et al., 2022). The method accounts for the finite thickness of the transition layer separating the mixed layer from the cloud layer above (Albright et al., 2022). This transition layer, approximately 150 m thick, complicates the application of classical mixed-layer theory which assumes an infinitesimally thin inversion.

The entrainment rate E is computed using a modified flux-jump model (Albright et al., 2022; Vogel et al., 2022) that extends the classical approach of Lilly (1968) and Stull (1976). ~~The entrainment rate represents the deepening of h due to~~ Within that diagnostic framework, E quantifies the exchange implied by small-scale mixing at the subcloud layer top and contributes to the tendency for h to deepen. This approach differs from the zero-order jump models that assume instantaneous transitions (Lilly, 1968) by accounting for the finite depth of the entrainment zone, providing a more realistic representation of the actual atmospheric structure observed during ~~EUREC4A~~EUREC^{4}A. Note that throughout this study, E refers only to entrainment from the cloudy layer (CL) into the subcloud layer (SCL). It does not include exchange between the CL and the free troposphere (FT). When E is used as an observational predictor or as a forcing coordinate in the synthetic mixed-layer model, it should be interpreted as a diagnosed cloud–subcloud exchange velocity rather than as a standalone prognostic equation for h. Negative diagnosed values indicate periods of interface descent or weak detrainment, not physically negative turbulent entrainment. None of the $n = 56$ complete matched cases used in the regressions below has negative E; the minimum matched value is $6.9\ \mathrm{mm\,s^{-1}}$. Across the matched circles, the average entrainment rate is $E = 18.8 \pm 6.9\ \mathrm{mm\,s^{-1}}$, and the average subcloud layer height is $h = 0.69 \pm 0.10$ km.

2.2 Isotopic and Surface Data

Water vapor isotope measurements aboard the R/V Meteor were obtained using a Picarro L2130-i cavity ring-down spectrometer (CRDS) operating at 1 Hz resolution from January 18 to February 22, 2020. The analyzer was housed in the Air-Chemistry Laboratory at ∼20.3 m above sea level, sampling ambient air through a 5 m long, 4.6 mm ID PTFE inlet line heated to 45°C and insulated with polyethylene foam. The inlet was housed in a downward-facing funnel to minimize contamination from rainwater and sea spray, and included a 0.2 μm PTFE aerosol filter. Flow was controlled by the CRDS system at approximately 0.03 slpm, resulting in a time delay of >2 minutes from intake to analyzer. Daily calibration checks were performed using four liquid water standards spanning δ^{18}O values from -20.97 to -2.79‰ and ~~δD~~ δD values from -158.13 to -13.12‰, delivered in gas phase using a Picarro Standards Delivery Module. Prior to normalization, isotopic observations were corrected for small humidity-dependent biases of up to 0.24‰ in δ^{18}O and 0.36‰ in ~~δD~~δD. Total uncertainties were estimated at 0.29‰ for δ^{18}O and 1.24‰ for ~~δD~~ δD by summing in quadrature the uncertainties associated with liquid standards, humidity-dependence correction, calibration measurement precision, and temporal drift over the campaign. Further details on the isotopic data collection program can be found in Bailey et al. (2023).

For the circle-based analysis, the shipboard Picarro observations were matched to the JOANNE Level 4 circle products by averaging quality-controlled δD and H_2O measurements within a 2-hour window centered on each circle time and within the fitted circle footprint. Of the 85 JOANNE Level 4 circles, 57 had matched ship-based isotope and humidity observations; requiring valid matched entrainment (E) and vertical velocity (W) estimates removes one additional circle, yielding the $n = 56$ complete cases used in the regressions below.

Near-surface relative humidity data were obtained from temperature and dew point measurements made at 29 m above the sea surface on the Meteor's mast. SST was measured at 2.3 m depth with matching port and starboard sensors.

3 Results

Figure 2 presents the full time series of surface water vapor measurements, relative humidity (RH), and sea surface temperature (SST) measured from the R/V *Meteor* during ~~EUREC4A~~EUREC^{4}A. The dataset exhibits ~~remarkably~~ relatively low variability across all measured parameters, reflecting the stable trade wind conditions that characterized the campaign period. Water vapor mixing ratios varied with a standard deviation of ~~only~~ 0.832 g kg^{-1} around a mean of 15.1 g kg^{-1}, while ~~δD~~ δD showed a standard deviation of 1.94‰ around a mean of -70.6‰. Surface meteorological ~~conditions were similarly constrained~~variability was also limited, with relative humidity varying by 4.6% around a mean of 71.6% and sea surface temperatures showing ~~minimal~~ little variation (standard deviation 0.23°C) around 27.3°C. The measurement uncertainty for 2-hour averaged isotope data (1.24‰ for ~~δD~~δD) represents approximately 65% of the observed natural variability, ~~constraining~~ limiting our ability to detect weak atmospheric signals. Consequently, our analysis focuses on the strongest and most robust correlations that exceed this measurement noise threshold.

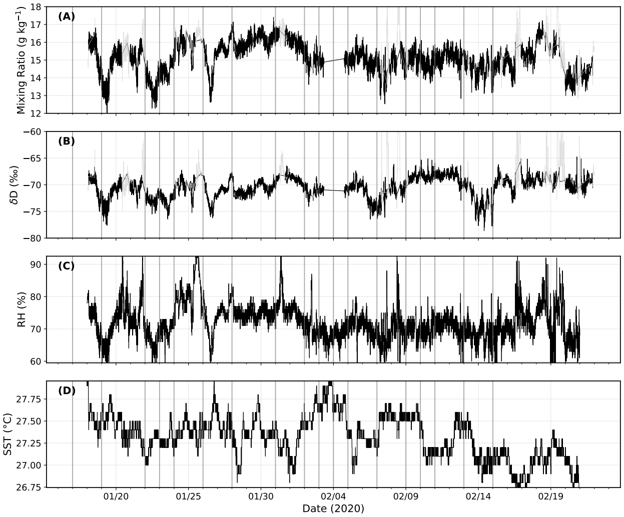

Figure 2. Time series of surface measurements from R/V *Meteor* during ~~EUREC4A~~EUREC^{4}A, January 18–February 22, 2020. (A) Water vapor mixing ratio from Picarro L2130-i cavity ring-down spectrometer at 1-minute resolution. (B) Deuterium isotope ratio (~~δD~~δD) from the same instrument. (C) Relative humidity from shipboard meteorological sensors. (D) Sea surface temperature. Black lines indicate quality-controlled data; pale gray points show measurements flagged during quality control. Gray vertical lines mark days with HALO/P3 aircraft circle flights from the JOANNE dropsonde dataset.

Figure ~~4 shows the vertical correlation structure between HALO-derived vertical velocity and surface isotopic composition (δD) and mixing ratio as a function of altitude relative to the top of the subcloud layer. Both δD (solid line) and mixing ratio (dashed line) exhibit their strongest correlations just below this boundary. The isotopic signal shows peak correlation ($r \approx 0.52$) about 100 meters below the top of the SCL, while humidity correlations reach maximum strength ($r \approx 0.39$) about 100 meters lower within the SCL. The enhanced correlations within this relatively narrow altitude range show that vertical velocity exerts its primary influence on surface humidity through processes operating near the top of the subcloud layer.~~

~~Vertical velocity correlation profiles with isotopic composition and humidity near subcloud layer height. Correlation coefficients between vertical velocity (W) and water vapor δ D (solid black line) and water vapor mixing ratio (dashed black line) are shown as functions of altitude relative to the top of the subcloud layer (SCL, red horizontal line at 0 m). The analysis spans ±500 m around the top of the SCL, which is defined as the height where virtual potential temperature first exceeds its density-weighted mean from 100 m by 0.2 K. Both variables show peak correlations within the subcloud layer, with δD exhibiting stronger coupling to vertical motion than humidity.~~

~~Figure~~ 3 shows (a) entrainment rate E (light blue) and vertical velocity W from ~~100~~ roughly 100–125 m below the top of the SCL (dark blue), both in mm s^{-1}; (b) surface ~~δ δD~~ δD in ‰; and (c) water vapor mixing ratio in g kg^{-1}. Each point represents a ~~6-hour~~ 2-hour average centered on a HALO/P3 circle time. The time series shows coherent variability across all of these parameters. Periods of enhanced entrainment (positive E values) consistently coincide with more negative ~~δD~~ δD and lower mixing ratio, as seen most clearly around January 26. Conversely, periods of weak entrainment or stronger mesoscale ascent (negative E, positive W) correspond to less negative ~~δD~~ δD and higher mixing ratios, evident around January 24 and February 1. Entrainment brings dry, isotopically depleted air from above the SCL into the surface layer, reducing humidity and driving ~~δD~~ δD toward more negative values (and overwhelming any potential increase in surface evaporation due to associated winds). Periods of reduced entrainment or mesoscale upward motion allow the boundary layer to maintain higher humidity and preserve the enriched isotopic signatures characteristic of ocean evaporation.

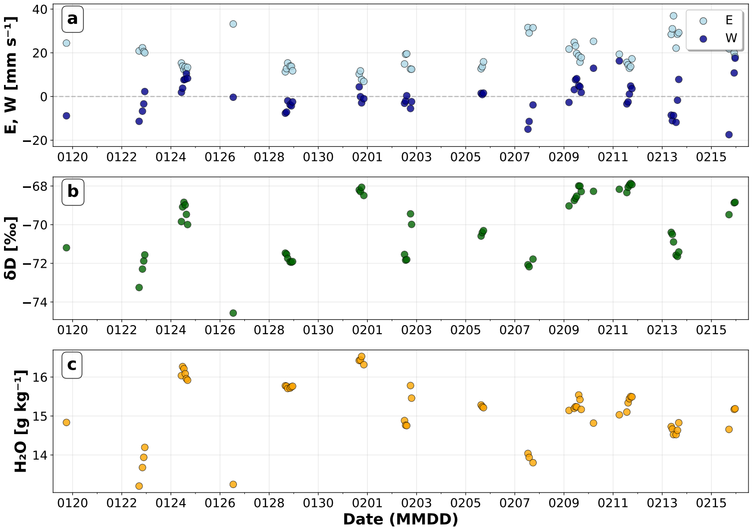

Figure 3. Time series of atmospheric variables during the ~~EUREC4A~~ EUREC^{4}A campaign. (a) Entrainment rate E (light blue) and mesoscale vertical velocity W from ~~100~~ roughly 100–125 m below the top of the SCL (dark blue) in mm s^{-1}, showing the competing effects of horizontal dry air mixing and convective vertical motion. The dashed gray line indicates zero. (b) Surface boundary layer ~~δD~~ δD in ‰, measured by the ship-based Picarro analyzer with an inlet at ∼20.3 m above sea level. (c) Water vapor mixing ratio H_2O in g kg^{-1} from matched ~~HALO-Picarro~~ HALO/P3-Picarro observations at the same inlet height. All data points represent 2-hour averaged values spatially matched within HALO/P3 flight circles. The time axis shows dates in MMDD format during ~~January-February~~ January–February 2020. Data demonstrate the temporal evolution of entrainment-convection competition and its effects on boundary layer moisture and isotope signatures.

~~This~~ Figure 4 shows the vertical correlation structure between dropsonde-derived vertical velocity and surface isotopic composition (δD) and mixing ratio as a function of altitude relative to the top of the subcloud layer. Both δD (solid line) and mixing ratio (dashed line) exhibit their strongest correlations just below this boundary. The isotopic signal shows peak correlation ($r \approx 0.52$) about 100–125 meters below the top of the SCL, while humidity correlations reach maximum strength ($r \approx 0.39$) about 100 meters lower within the SCL.

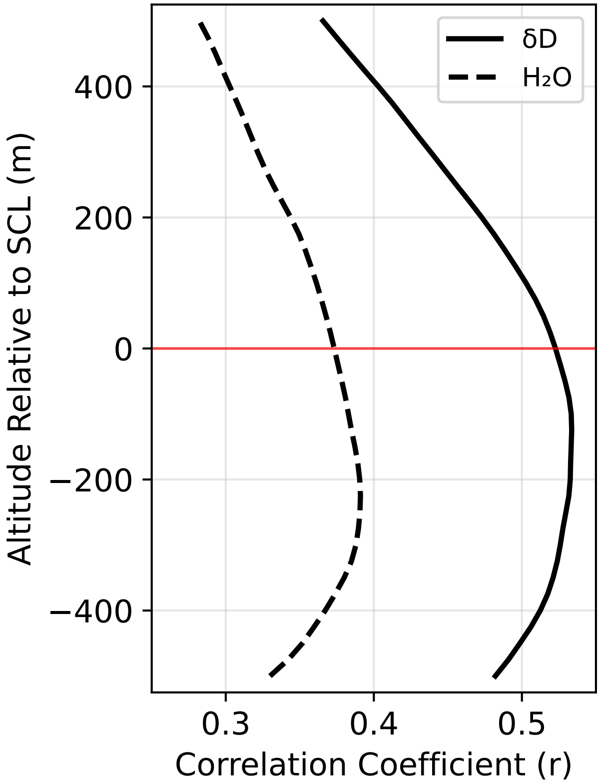

Figure 4. Vertical velocity correlation profiles with isotopic composition and humidity near subcloud layer height. Correlation coefficients between vertical velocity (W) and water vapor δD (solid black line) and water vapor mixing ratio (dashed black line) are shown as functions of altitude relative to the top of the subcloud layer (SCL, red horizontal line at 0 m). The analysis spans ±500 m around the top of the SCL, which is defined as the height where virtual potential temperature first exceeds its density-weighted mean from 100 m by 0.2 K. Both variables show peak correlations within the subcloud layer, with δD exhibiting stronger coupling to vertical motion than humidity.

This structure is further illustrated in Figure 5, which shows the relationship between vertical velocity ~~W~~ W (x-axis) and entrainment rate ~~E~~ E (y-axis), with points colored by surface ~~δD values~~ δD and sized according to water vapor mixing ratio. The scatter plot ~~shows~~ reveals a systematic organization of boundary layer states across the ~~E-W~~ E–W parameter space. Points in the ~~upper left~~ upper-left quadrant (negative ~~W, high E) represent~~ W, high E) correspond to conditions of strong entrainment combined with ~~downdrafts,~~ mesoscale downdrafts and are characterized by more negative ~~δD values and low~~ δD values and lower mixing ratios. Points toward the lower right (positive ~~W, low E~~ W, low E) indicate periods of ~~weak entrainment and stronger~~ weaker entrainment and mesoscale ascent, which are associated with ~~higher δD values and higher mixing ratios. This figure demonstrates that E and W are not entirely~~ less negative δD values and modestly higher humidity.

A linear regression across all matched circles ($n = 56$) yields

$$E = -0.25W + 18.6, \tag{1}$$

with a statistically significant negative slope ($p = 0.044$, 95% confidence interval $[-0.49, -0.01]$), indicating that entrainment and vertical velocity are weakly but systematically anticorrelated. Although this relationship exhibits substantial scatter, it demonstrates that E and W are not independent but instead ~~define~~ span a continuum of boundary layer mixing states. ~~The color gradient from dark (depleted) to light (enriched) δD values follows a clear diagonal pattern from high E, negative W conditions toward low E, positive W conditions. Similarly, marker~~

Consistent with this organization, the δD color gradient transitions from more depleted values under high-E, negative-W conditions toward more enriched values under low-E, positive-W conditions. Marker sizes increase along this same trajectory, indicating that periods of reduced entrainment and ~~upward motion coincide with both~~ mesoscale ascent coincide with isotopic enrichment and enhanced humidity.

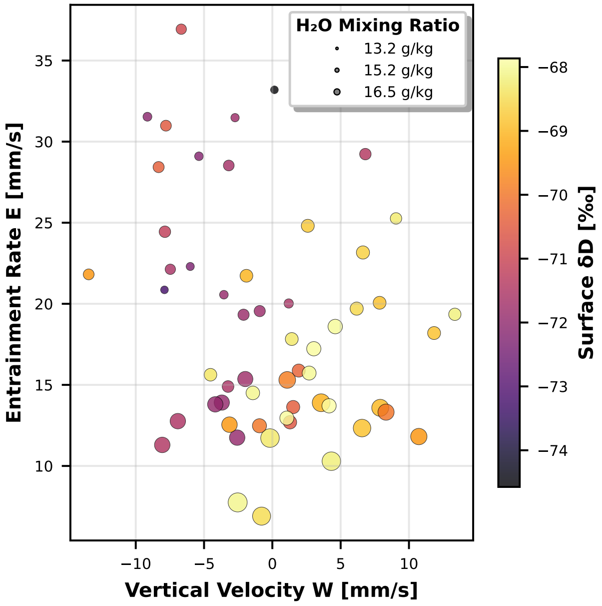

Figure 5. Relationships between vertical velocity (W), entrainment rate (E), water vapor mixing ratio, and water vapor ~~δD~~ δD during ~~EUREC4A~~EUREC^{4}A. Scatter plot shows W extracted at ~~optimal~~ the empirically selected absolute altitude of maximum δD–W correlation from Figure 4 (567.7 m above the sea surface) versus entrainment rate E, with circle size proportional to water vapor mixing ratio (H_2O) and color representing surface ~~δD~~δD. Data points represent individual dropsonde circles matched with ship-based isotope measurements.

A more quantitative understanding of these relations is illustrated in Figs. 6 and 7. Figure 6 shows the joint dependence of isotopic composition and humidity on both entrainment and vertical velocity. Panel (A) shows ~~δD~~ δD values across the E-W parameter space, with contour lines representing predictions from a joint linear regression model that includes both E and W as predictors. The isotopic field exhibits a systematic gradient from depleted values (~~δD~~ $\delta D \approx$ -73‰) at high entrainment rates and negative vertical velocities to enriched values (~~δD~~ $\delta D \approx$ -68‰) at low entrainment and positive vertical velocities. Panel (B) shows the corresponding humidity field, where water vapor mixing ratios decrease from approximately 16.5 g kg^{-1} at low ~~E and high W~~ E and high W to 13.5 g kg^{-1} at high ~~E and low W. The~~ E and low W. To quantify these relationships, we performed a joint multilinear regression for both variables. The regression for δD yields $\delta D = -0.071E + 0.100W - 68.74$ ($R^2 = 0.357$), where both predictors are statistically significant at the 5% level ($p \approx 0.013$ for E and $p \approx 0.00027$ for W), with a residual mean absolute error (MAE) of 1.15‰ and an RMSE of 1.33‰. For specific humidity, the regression yields $H_2O = -0.083E + 0.019W + 16.72$ ($R^2 = 0.633$), with coefficients that are also significant ($p \approx 2.5 \times 10^{-11}$ for E and $p \approx 0.040$ for W) and a residual MAE of 0.365 g kg^{-1} and RMSE of 0.472 g kg^{-1}. These results quantify the “diagonal” structure seen in the parameter space, demonstrating that both predictors are statistically significant, with a moderate fit for δD and a stronger fit for H_2O. The orientation of the contours in both panels ~~shows that δD~~ further confirms that δD is more sensitive to ~~W~~ W than the total mixing ratio, which is more sensitive to entrainment. For clarity, throughout this paper we define contour angle as the angle of the fitted contour line measured counterclockwise from the $+E$ axis. Under this convention, the observational fitted contour angles are 35.5° for δD and 77.0° for humidity, giving an observational contour separation of 41.5°.

In interpreting these results, we note that E and W are not independent predictors; in our dataset, they exhibit a modest negative correlation ($r \approx -0.27$). However, the joint multilinear regression framework used here specifically accounts for this covariance. The reported MLR coefficients represent partial slopes, quantifying the independent impact of each variable while holding the other constant. Consequently, the distinct point-estimate sensitivities observed for δD and humidity are not simply artifacts of the correlation between entrainment and vertical motion, although the magnitude of the resulting counteraction-efficiency contrast remains uncertainty-limited.

Figure 7 further quantifies the counteraction effect of ~~W on E~~ mesoscale vertical velocity (W) on entrainment (E) through residual analysis. This approach first removes the linear effect of entrainment alone, then ~~quantifies~~ examines how vertical velocity correlates with the remaining variance. ~~The δD~~ Using the full dataset ($n = 56$), the fully standardized regression coefficients for δD are $\beta_E = -0.295$ and $\beta_W = +0.446$. For humidity, the fully standardized coefficients are $\beta_E = -0.727$ and $\beta_W = +0.182$. These coefficients are obtained from the joint regression and do not assume independence between E and W.

The δD residuals (Panel~~A) show~~ A) exhibit a strong positive correlation with ~~W (r = 0.464~~ W ($r = 0.464$), indicating that upward motion systematically counteracts entrainment-driven ~~depletion. The counteraction efficiency is defined~~ isotopic depletion. We define a counteraction efficiency metric as the ratio of the ~~W regression slope to the E regression slope and reaches 1.19 for δD, meaning that 1~~ absolute values of the standardized regression coefficients,

$$\eta = \left|\frac{\beta_W}{\beta_E}\right|, \tag{2}$$

which quantifies the relative statistical influence of mesoscale ascent and entrainment in units of standard deviations. For δD, this yields $\eta_{\delta D} \approx 1.5$, whereas for humidity the corresponding point estimate is much smaller, $\eta_q \approx 0.25$. Because η is itself

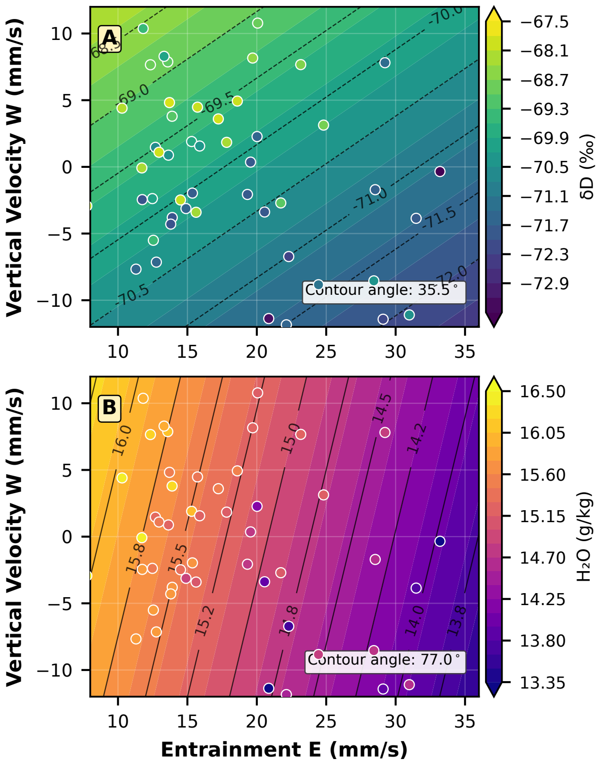

Figure 6. Joint entrainment-vertical velocity dependencies in isotopic composition and humidity fields. (A) Contour plot showing water vapor ~~δ D~~ δD as a function of entrainment rate E and vertical velocity W, with observations overlaid as colored points. Contour lines represent predictions from the joint E-W regression model. (B) Water vapor mixing ratio (~~H2O~~H_2O) dependencies on the same E-W parameter space, using a different color scheme to distinguish variables.

a ratio of two estimated coefficients, its uncertainty is broader and more asymmetric than the uncertainties on the individual slopes; the bootstrap 95% confidence interval for $\eta_{\delta D}$ spans roughly 0.50–12.86. Thus, the data do not precisely constrain the numerical value of $\eta_{\delta D}$, rule out values below unity, or exclude the possibility that the apparent difference between the δD and humidity counteraction efficiencies is smaller than implied by the point estimates. We therefore interpret the efficiency contrast as suggestive rather than statistically resolved.

Because this metric is based on standardized coefficients, it does not represent cancellation in physical units (mm s^{-1}~~of upward motion counteracts the isotopic effect of 1.19~~), but instead compares the sensitivity of each variable to variability in the two predictors. Physical cancellation in mm s^{-1} can instead be assessed using the unstandardized regression slopes. From the fitted relationship

$$\delta D = -0.071\,E + 0.100\,W - 68.74, \tag{3}$$

we find that approximately 0.7 mm s^{-1} of mesoscale ascent is required to offset the isotopic impact of 1 mm s^{-1} of entrainment. For ~~water vapor (Panel B), the counteraction is weaker, with r = 0.270 and an efficiency of 0.30. Mesoscale vertical velocities exerts a much stronger control on isotopic composition than on humidity itself. The efficiency greater than unity for δD indicates~~ humidity, the corresponding unstandardized slopes imply that approximately 4.4 mm s^{-1} of mesoscale ascent would be required to offset the drying associated with 1 mm s^{-1} of entrainment.

The point estimates of counteraction efficiency suggest that mesoscale processes ~~dominate over entrainment in determining surface isotopic signatures, while the much lower efficiency for humidity reflects the more equitable relationship between vertical motion and entrainment in setting the~~ exert a stronger relative influence on isotopic variability than entrainment alone, whereas the lower point estimate for humidity implies a weaker role of vertical motion in setting boundary-layer water vapor concentrations~~in the boundary layer. While these correlations~~. Although these relationships exceed the noise threshold identified earlier, ~~we note that the measurement uncertainty represents~~ measurement uncertainty constitutes a large fraction of the observed ~~δD variance. Thus~~δD variance. As a result, the precise values of the regression slopes and efficiencies should be interpreted ~~with caution, even though the qualitative pattern of a stronger isotopic than humidity response is robust~~cautiously, and the data do not rule out a smaller or statistically indistinct difference between the isotopic and humidity counteraction efficiencies.

These results ~~demonstrate~~ show that mesoscale circulations significantly modulate the entrainment-driven changes in boundary layer humidity and composition, consistent with the findings of Vogel et al. (2022) and George et al. (2023). The isotopic measurements provide quantitative constraints on the relative importance of these competing processes, with mesoscale vertical motions capable of fully offsetting or even reversing entrainment effects on ~~boundary layer moisture characteristics~~boundary-layer δD.

3.1 ~~Mixed Layer~~ Flux-Form Mixed-Layer Model

~~To better understand the processes responsible for the asymmetric responses of δD and q to entrainment and mesoscale vertical motion, we implemented a steady-state flux-form mixed-layer model (Appendix ??)~~The observational analysis above establishes that δD responds more strongly than humidity to mesoscale vertical velocity, but it does not identify the physical mechanism responsible for this asymmetry. Warm rain and cold-pool signatures are common in the trade-wind regime, and EUREC^{4}A observations document precipitation and cold-pool influences on the subcloud layer (Touzé-Peiffer et al., 2022; Radtke et al., 20 . Previous observational and modeling studies have established that below-cloud evaporation is an important term in tropical water-isotope budgets, because falling droplets can return condensate-derived heavy isotopes to unsaturated subcloud air (Tremoy et al., 2014; Graf et al., 2019; Risi et al., 2020). Crucially, rain evaporation adds moisture and isotopic mass simultaneously, but the isotopic ratio of the evaporated vapor differs from that of the ambient subcloud vapor due to fractionation during partial evaporation. If the rain-evaporation moisture flux is modest relative to the full subcloud moisture budget, this process can strongly affect δD while producing only a weak humidity response.

To test this hypothesis, we developed a prognostic control-volume model that resolves the competing fluxes governing subcloud layer humidity and isotopic composition. The model ~~represents the boundary~~ treats the subcloud layer as a ~~single,~~

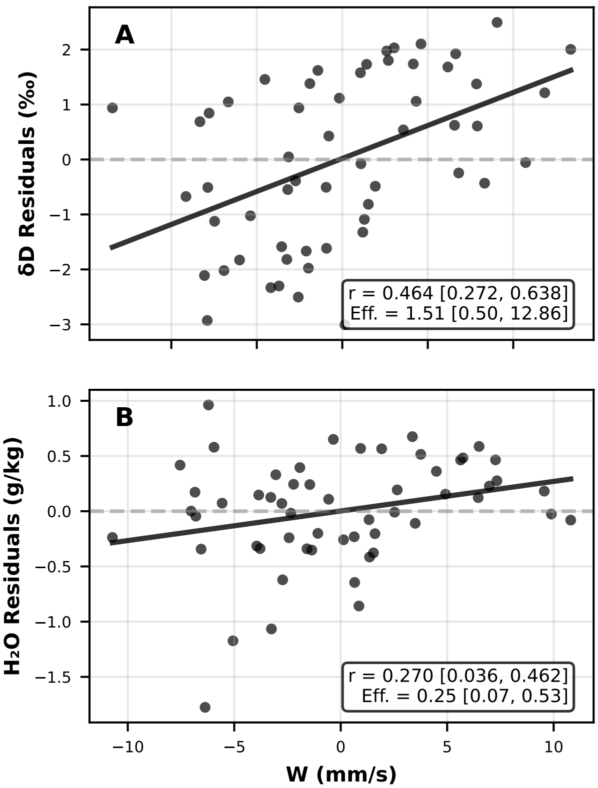

Figure 7. Residual analysis of vertical velocity counteraction effects on isotopic composition and humidity. (A) ~~ΔD~~ δD residuals after removing entrainment-only effects plotted against vertical velocity W at optimal altitude. Points show individual HALO/P3 circle observations, with the regression line indicating the pure counteraction effect of W. The correlation coefficient (r) and counteraction efficiency (Eff.) quantify how effectively vertical motion counteracts entrainment-driven isotopic depletion. (B) Water vapor mixing ratio (~~H2O~~H_2O) residuals after removing entrainment-only effects plotted against vertical velocity W.

well-mixed slab ~~in which water vapor and its isotopic composition are determined by the balance between~~ of prescribed depth h and air density ρ that exchanges mass and isotopic mass with three reservoirs: the ocean surface, the overlying cloudy layer, and a rain evaporation source whose strength depends on mesoscale vertical velocity. All fluxes enter both the moisture and isotopic budgets explicitly; there is no term that modifies isotopic composition without a corresponding mass flux.

3.1.1 Conserved-variable framework

The model advances two prognostic variables: the column water-vapor inventory $Q = \rho h q$ and the column heavy-isotopologue vapor inventory $M_D = \rho h q R$, where q is the specific humidity and $R = [\mathrm{HDO}]/[\mathrm{H_2O}]$ is the isotopic ratio. These inventories represent the mass stored in the well-mixed subcloud control volume per unit horizontal area. The budget equations are

$$\frac{dQ}{dt} = F_{\rm surf} + F_{\rm ent} + F_{\rm rain}, \tag{4}$$

$$\frac{dM_D}{dt} = F_{{\rm surf},D} + F_{{\rm ent},D} + F_{{\rm rain},D}, \tag{5}$$

where the three flux terms on the right-hand side represent surface evaporation, ~~turbulent~~ entrainment from the cloudy layer, and ~~large-scale vertical motions. Surface evaporationis parameterized using Craig–Gordon theory,~~ rain evaporation, respectively. In the synthetic equilibrium experiments presented here, h is held fixed, so E is interpreted as the cross-interface exchange velocity across this prescribed control volume rather than as a prognostic deepening rate for h. The specific humidity and isotopic ratio are recovered diagnostically as $q = Q/(\rho h)$ and ~~entrainment is prescribed as an independent flux of mass~~ $R = M_D/Q$. Isotopic ratios are reported in standard delta notation, $\delta D = 1000(R/R_{\rm VSMOW} - 1)$, where $R_{\rm VSMOW} = 155.76 \times 10^{-6}$.

By formulating the budgets in terms of Q and ~~isotopes from the overlying air. Mesoscale vertical velocity influences the model both directly, by modulating the net mass budget of the mixed layer ,~~ M_D rather than q and ~~indirectly, by altering the effective entrainment rate. This simple framework captures the observed contrast in sensitivity, with δD responding much more strongly than q to variations in mesoscale vertical motion, thereby providing a mechanistic interpretation of the asymmetries seen in the observations~~R directly, the model avoids the nonlinear coupling and potential numerical inconsistencies that arise when isotopic ratio equations are solved independently of the mass budget. This conserved-variable approach ensures that the isotopic budget is strictly consistent with the mass budget at every timestep.

3.1.2 Surface evaporation

The surface moisture flux is parameterized using bulk aerodynamic theory:

$$F_{\rm surf} = \rho C_E U (q_{\rm sat} - q), \tag{6}$$

where C_E is the bulk transfer coefficient, U is the surface wind speed, and $q_{\rm sat}$ is the saturation specific humidity at sea surface temperature and surface pressure. The corresponding isotopic flux follows the Craig–Gordon formulation (Craig and Gordon, 1965) :

$$F_{{\rm surf},D} = \rho C_E U \left(\frac{q_{\rm sat} R_{\rm oc}}{\alpha_{\rm eq} \alpha_k} - \frac{q R}{\alpha_k} \right), \tag{7}$$

where $R_{\rm oc}$ is the isotopic ratio of ocean surface water, $\alpha_{\rm eq}$ is the temperature-dependent equilibrium fractionation factor (Majoube, 1971), and α_k is the kinetic fractionation factor associated with diffusive transport through the interfacial sublayer (Merlivat and Jouzel, 1979).

This formulation deserves brief comment. The classical Craig–Gordon model expresses the isotopic ratio of the evaporating vapor as a function of relative humidity $H = q/q_{\rm sat}$, with a $(1 - H)$ factor in the denominator that produces a singularity as $H \to 1$. However, when the evaporative isotopic flux is written as the product of the mass flux F_{surf} and the evaporating vapor's isotopic ratio, the $(1-H)$ factors cancel exactly between the mass flux and the Craig–Gordon expression. Equation (7) implements this cancelled form directly, ensuring that the isotopic flux remains well-defined and proportional to F_{surf} across all humidity conditions.

3.1.3 Entrainment

Entrainment from the cloudy layer into the subcloud layer is parameterized as

$$F_{\mathrm{ent}} = \rho\, E\, (q_{\mathrm{CL}} - q), \tag{8}$$

$$F_{\mathrm{ent},D} = \rho\, E\, (q_{\mathrm{CL}}\, R_{\mathrm{CL}} - q\, R), \tag{9}$$

where E is the entrainment velocity (m s^{-1}), and q_{CL} and R_{CL} are the specific humidity and isotopic ratio of the cloudy layer, respectively. Because $q_{\mathrm{CL}} < q$ in the trades, entrainment acts as a moisture sink and, because the cloudy layer is isotopically depleted relative to the subcloud layer ($R_{\mathrm{CL}} < R$), it simultaneously depletes δD. The isotopic flux is written in terms of the conserved quantity qR rather than R alone, maintaining strict consistency with the mass budget.

3.1.4 Rain evaporation

The rain evaporation term is the additional process tested as a mechanism for the observed asymmetry. As raindrops formed by condensation in the cloud layer fall through the unsaturated subcloud layer, they partially evaporate. This process adds both mass and isotopic mass to the subcloud vapor, but the isotopic ratio of the evaporated vapor differs from that of the ambient vapor because of fractionation during partial evaporation.

~~Figure ?? shows the sensitivity of modeled boundary-layer humidity (q) and isotopic composition (δD) to~~ The rain evaporation mass flux is

$$F_{\mathrm{rain}} = f(W) \cdot P_{\mathrm{cb}} \cdot \chi, \tag{10}$$

where P_{cb} is a reference cloud-base precipitation-rate scale (kg m^{-2} s^{-1}), χ is the fraction of the falling rain mass that evaporates before reaching the surface, and $f(W)$ is a rain activity function that modulates the effective precipitation input with mesoscale vertical velocity W. Equivalently, the effective mean cloud-base precipitation input is $P_{\mathrm{cb,eff}}(W) = f(W)P_{\mathrm{cb}}$. The corresponding isotopic flux is

$$F_{\mathrm{rain},D} = F_{\mathrm{rain}} \cdot R_{\mathrm{ev}}, \tag{11}$$

where R_{ev} is the isotopic ratio of the vapor produced by rain evaporation.

The rain activity function $f(W)$ represents the dependence of precipitation activity on mesoscale vertical velocity. Mesoscale ascent is associated with cloud organization and cloudier, moister mesoscale states (George et al., 2023; Vogel et al., 2022), so we use W ~~, expressed in standardized units to facilitate comparison. For each variable, anomalies are computed relative to~~

~~the model state at $W = 0$ and then normalized by the corresponding standard deviation from the observational campaign ($\sigma_q = 0.832$ g kg^{-1}, $\sigma_{\delta D} = 1.94$ ‰). Expressing the results in these σ units allows a direct comparison of the relative strength of the W-induced changes in q and δD despite their different physical units and variances. A slope of unity in these units would correspond to a change equal to one observed standard deviation per 1 cm s^{-1} change in W.~~ as a coordinate for the precipitation flux that can drive below-cloud evaporation. We parameterize this dependence as a logistic function,

$$f(W) = \frac{1}{1 + \exp(-W/W_{\mathrm{width}})}, \tag{12}$$

where W_{width} controls the sharpness of the transition between suppressed and active precipitation regimes. This function varies smoothly from near zero for strong subsidence to near unity for strong ascent, with the midpoint at $W = 0$. The specific functional form is a modeling choice rather than a universal precipitation law, but assigning larger effective precipitation input during mesoscale ascent is physically motivated by the observed cloud–circulation coupling during EUREC^{4}A (George et al., 2023; Vogel e

.

~~Sensitivity of boundary-layer mixing ratio (q) and isotopic composition (δD) to mesoscale vertical velocity from the flux-form mixed-layer model. Curves show anomalies of δD (solid) and q (dashed) expressed in observational σ units versus vertical velocity W (cm,s^{-1}), at fixed entrainment $E = 20$,mm,s^{-1}.~~

~~The curves in Figure **??** exhibit a clear asymmetry in the modeled responses. For $W > 0$ (mesoscale ascent)~~

3.1.5 Below-cloud isotopic fractionation

The isotopic ratio of the vapor released by partial rain evaporation, R_{ev}, is computed using the below-cloud evaporation model of Stewart (1975). This model tracks the evolution of a raindrop's isotopic composition as it falls through unsaturated air, accounting for both equilibrium fractionation at the drop surface and kinetic fractionation during diffusive transport of vapor away from the drop.

The raindrop is assumed to form at cloud base by equilibrium condensation from cloud-layer vapor, giving an initial liquid isotopic ratio $R_{r,\mathrm{cb}} = \alpha_{\mathrm{eq}}(T_{\mathrm{cb}}) \cdot R_{\mathrm{CL}}$, where $\alpha_{\mathrm{eq}}(T_{\mathrm{cb}})$ is the equilibrium fractionation factor at cloud-base temperature. Here and in the surface-flux formulation above, α_{eq} denotes the liquid-to-vapor equilibrium fractionation factor, so $\alpha_{\mathrm{eq}} > 1$. Because liquid is enriched relative to vapor in equilibrium, $R_{r,\mathrm{cb}} > R_{\mathrm{CL}}$: the raindrop starts with a higher isotopic ratio than the cloud-layer vapor from which it formed.

As the drop partially evaporates, the isotopic ratio of the remaining liquid evolves according to (Stewart, 1975):

$$R_{r,\mathrm{sfc}} = \gamma R + (R_{r,\mathrm{cb}} - \gamma R)\mathfrak{f}^{\beta}, \tag{13}$$

where $\mathfrak{f} = 1 - \chi$ is the fraction of the original drop mass that survives to the surface, R is the ambient vapor isotopic ratio, and γ and β are functions of the equilibrium fractionation factor α_{eq}, the molecular diffusivity ratio D/D', the kinetic exponent n, and the ambient relative humidity H:

$$\kappa = \alpha_{\rm eq}\left(\frac{D}{D'}\right)^{n}(1-H), \tag{14}$$

$$\beta = \frac{1-\kappa}{\kappa}, \tag{15}$$

$$\gamma = \frac{\alpha_{\rm eq}H}{1-\kappa}. \tag{16}$$

The isotopic ratio of the total vapor released by evaporation is then obtained by mass balance over the evaporated fraction:

$$R_{\rm ev} = \frac{R_{r,\rm cb} - \mathfrak{f}R_{r,\rm sfc}}{1-\mathfrak{f}}. \tag{17}$$

This formulation captures the leading-order isotope mass balance associated with below-cloud evaporation. For the conditions typical of the EUREC^{4}A subcloud layer ($H \approx 0.7$, ~~both q and~~ $T_{\rm cb} \approx 18\,^\circ$C, $\chi \approx 0.8$), the evaporated vapor is isotopically enriched relative to the ambient subcloud vapor. With the baseline parameters, the cloud-base liquid has $\delta D_{r,\rm cb} \approx +2.6$‰ and the mass-weighted evaporated vapor has $\delta D_{\rm ev} \approx -10$‰, about 60‰ enriched relative to the ambient subcloud vapor. The enrichment arises because the raindrop starts with a high isotopic ratio (set by equilibrium condensation from cloud-layer vapor) and, during partial evaporation, preferentially loses light molecules. The vapor released is therefore enriched relative to both the cloud-layer vapor from which the drop formed and the ambient subcloud vapor into which it evaporates. This enrichment provides a mechanism for the asymmetric response: rain evaporation during mesoscale ascent adds vapor that is isotopically distinct from the ambient subcloud air, strongly modifying δD~~increase, while for $W<0$ (descent) they decrease. However, the magnitude of~~, while the ~~response in δD is much larger: the model yields a linear sensitivity of about 3.72 $\sigma_{\delta D}$ per cm~~ mass of moisture added by rain evaporation is small relative to the total subcloud moisture budget, producing only a modest change in q.

3.1.6 Model integration and equilibrium structure

The model is integrated forward in time with a 20 s timestep from specified initial conditions until a quasi-steady state is reached (typically 60 hours of integration, with results averaged over the final 24 hours). For a given pair of forcing values (E, W), the model evolves toward an equilibrium in which the surface evaporation, entrainment, and rain evaporation fluxes balance. We compute the equilibrium state across a grid spanning the observed range of entrainment rates ($E = 10$–35 mm s^{-1}~~, compared to only 0.49 σ_q per cm~~) and vertical velocities ($W = -10$ to $+10$ mm s^{-1}~~for q, a ratio of roughly 7.5. This difference reflects the fact that~~).

We represent below-cloud rain evaporation as a steady drizzle source whose effective mean input is modulated by $f(W)$. This mean-flux representation is appropriate for diagnosing the equilibrium response: the question is not the detailed timing of rain events, but whether a W-dependent source of fractionated rain evaporation can rotate the δD ~~is sensitive not only to changes in total water mass but also to shifts in the isotopic composition of the entrained air.In the model, mesoscale ascent~~

~~reduces the relative contribution of isotopically depleted CL air, driving~~ contours relative to the humidity contours. The model does not include a separate direct vertical-advection term proportional to W; instead, W is used as a forcing coordinate for the rain-activity pathway being tested. We therefore compare the drizzle case with a no-rain control in which $F_{\mathrm{rain}} = F_{\mathrm{rain},D} = 0$.

Figure 8 shows the resulting equilibrium structure. Using the same contour-angle convention as in Fig. 6, the drizzle case yields fitted δD ~~upward, while mesoscale descent enhances the entrainment influence and lowers δD. Because q is controlled solely by~~ contours with an angle of 31.0° in the E–W plane, whereas the fitted q contours have an angle of 66.5°, giving a contour separation of 35.4°. Equivalently, the ~~net mass fluxes, its fractional changes are smaller.~~ ratio of the fitted W and E sensitivities is much larger for isotopic composition ($|\partial\delta D/\partial W|/|\partial\delta D/\partial E| = 1.66$) than for humidity ($|\partial q/\partial W|/|\partial q/\partial E| = 0.44$). Thus, rain evaporation produces a state in which δD is strongly modulated by mesoscale vertical velocity while q remains primarily controlled by entrainment. In the no-rain control, both variables have nearly vertical fitted contours and zero W sensitivity, so the contour separation collapses. The modeled separation is somewhat smaller than the observational separation of $41.5°$, but the two are close enough to support the same qualitative interpretation. This comparison shows that below-cloud rain evaporation is a process that can generate the non-parallel q–δD structure.

~~This modeled behavior parallels the observational results: in both, the isotopic composition responds much more strongly to mesoscale vertical motion than does humidity,~~

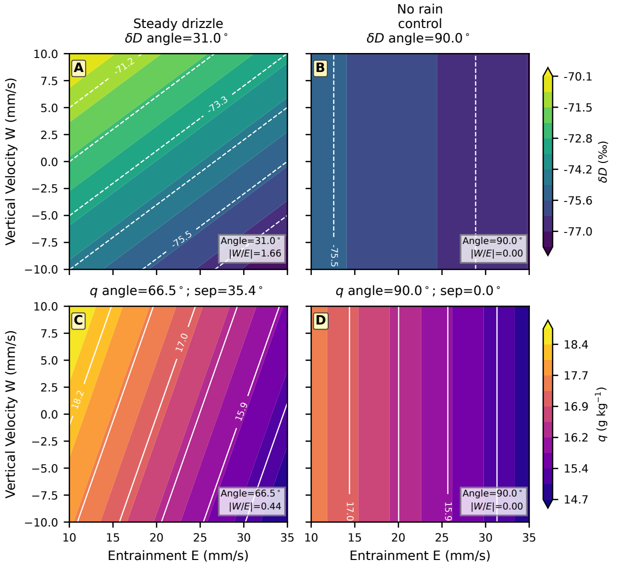

Figure 8. Modeled equilibrium structure across the entrainment–vertical velocity (E–W) parameter space. Panels (A) and (B) show fitted-plane δD fields for the steady-drizzle case and the no-rain control, respectively. Panels (C) and (D) show the corresponding fitted-plane humidity fields. White lines show contours of the fitted planes. In the drizzle case, δD contours rotate strongly toward W sensitivity while q remains more E-dominated; in the no-rain control, both fields collapse to nearly E-only structure.

3.1.7 Parameter values

The model parameters are summarized in Table 1. Environmental conditions are set to campaign-mean values: SST $= 27.3\,^{\circ}$C, surface pressure $p = 1013.25$ hPa, subcloud layer depth $h = 700$ m, and surface wind speed $U = 8$ m s^{-1}. The bulk transfer coefficient $C_E = 1.2 \times 10^{-3}$ is a standard value for open-ocean conditions. Equilibrium fractionation follows Majoube (1971). For the surface Craig–Gordon flux, kinetic fractionation uses $\alpha_k = (D/D')^n$ with $D/D' = 1.0159$. For the Stewart below-cloud evaporation calculation, we use the deuterium diffusivity ratio $D/D' = 1.024$ and ~~the sign of the response is~~ $n = 0.58$ (Merlivat and Jouzel,
.

The cloudy-layer end member is specified as $q_{\mathrm{CL}} = 13.0$ g kg^{-1} and $\delta D_{\mathrm{CL}} = -78$‰, consistent with the ~~balance between surface evaporation and entrainment from the CL. The σ-unit scaling underscores that the stronger isotope response is not an artifact of measurement units, but reflects a genuinely greater fraction of~~ mean dropsonde profiles. The cloud-base temperature is set to $T_{\mathrm{cb}} = 18\,^{\circ}$C, and the ~~observed variability being explained by W in~~ ocean isotopic ratio to $\delta D_{\mathrm{oc}} = 0$‰.

The rain evaporation parameters—reference cloud-base precipitation-rate scale $P_{\mathrm{cb}} = 5 \times 10^{-5}$ kg m^{-2} s^{-1}, evaporated fraction $\chi = 0.8$, and logistic width $W_{\mathrm{width}} = 4$ mm s^{-1}—are free parameters, not independently fitted observations. We choose them to represent weak trade-cumulus drizzle: the precipitation-rate scale is consistent with observed trade-cumulus rain rates (Radtke et al., 2022), and the high evaporated fraction reflects the shallow cloud base and warm subcloud conditions, in which much of the falling precipitation can evaporate before reaching the surface. The fixed evaporated fraction is a bulk simplification; the model does not resolve drop-size distributions, ventilation, or vertical variations in relative humidity and temperature along the fall path.

Figure 9 shows a targeted two-parameter sensitivity sweep spanning (P_{cb}, χ) at fixed $W_{\mathrm{width}} = 4$ mm s^{-1}. The baseline configuration used throughout the paper is marked on each panel. The upper-left panel shows the modeled contour separation between δD ~~than in q. This asymmetry emerges naturally from the model physics, without requiring any ad hoc tuning,~~ and ~~provides a simple mechanistic explanation for the patterns seen in the data.~~ q, the upper-right and lower-left panels show the corresponding W-to-E sensitivity ratios for humidity and isotopic composition, and the lower-right panel shows the absolute mismatch between the modeled and observed contour separations. The baseline point lies in the regime where δD is clearly W-sensitive ($|\partial \delta D/\partial W|/|\partial \delta D/\partial E| > 1$) while humidity remains E-dominated ($|\partial q/\partial W|/|\partial q/\partial E| < 1$), and it yields a modeled contour separation close to the observed value. Because W_{width} controls the shape of the prescribed W–rain transition rather than the rain-flux amplitude, we also ran a baseline-only sensitivity check over $W_{\mathrm{width}} = 2$–8 mm s^{-1} (not shown). For $W_{\mathrm{width}} = 2$–6 mm s^{-1}, the model retains the qualitative target of W-sensitive δD and E-dominated humidity, with contour separations of approximately 33–36°; a broader transition of 8 mm s^{-1} weakens the isotope W sensitivity to near unity and reduces the separation to about 30°.

The figure also shows why the parameter choice cannot be increased arbitrarily. Moving toward larger P_{cb} and χ strengthens the isotopic response further, but it also increases the humidity response to W and reduces the separation between the humidity and isotope contours. In other words, sufficiently strong rain evaporation rotates both fields and degrades the observed q–δD

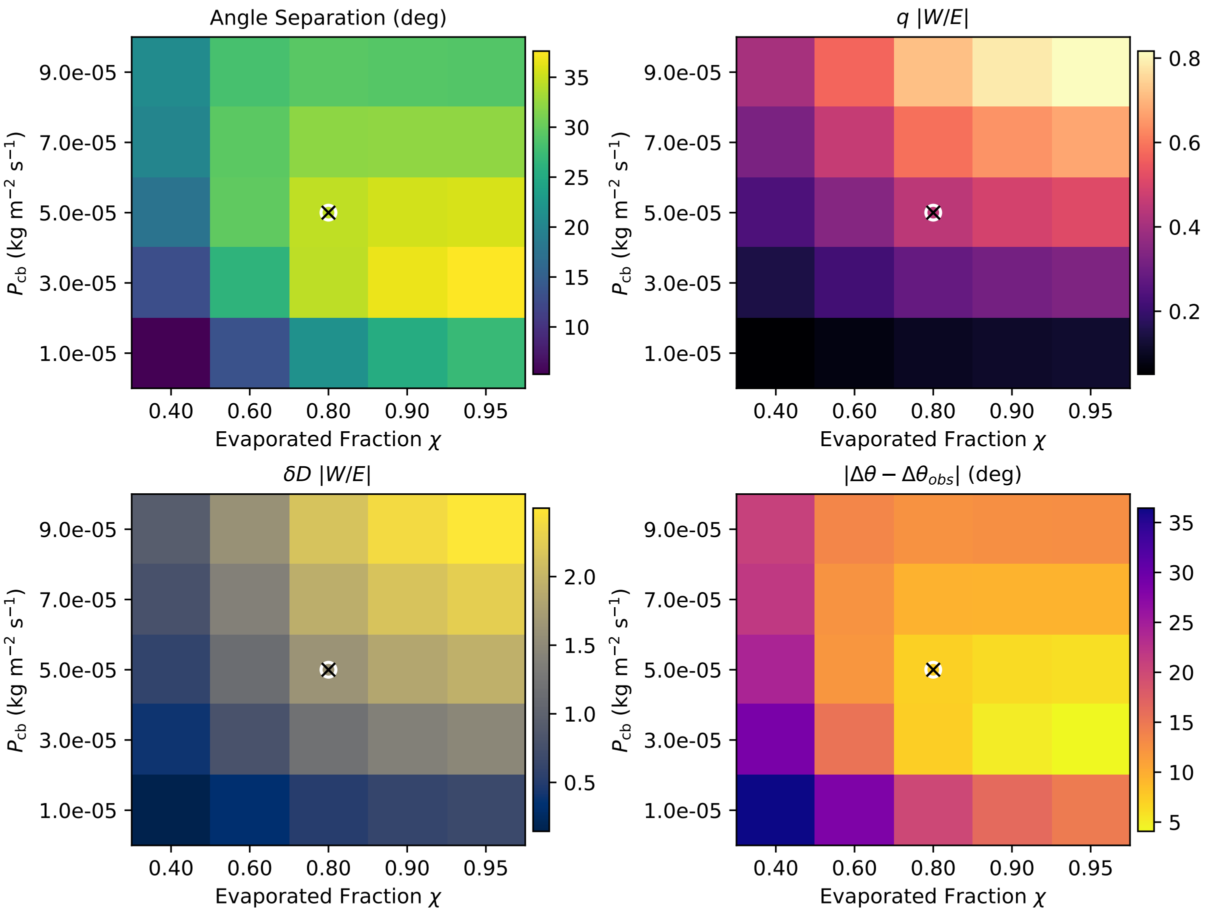

Figure 9. Targeted sensitivity of the steady-drizzle model to the reference cloud-base precipitation-rate scale P_{cb} and evaporated rain fraction χ at fixed $W_{\mathrm{width}} = 4$ mm s^{-1}. Panels show the modeled contour separation between δD and q, the corresponding W-to-E sensitivity ratios for humidity and δD, and the misfit relative to the observed contour separation. The marker denotes the baseline drizzle configuration used in the main text.

asymmetry. The qualitative model result is therefore robust to moderate parameter perturbations, but it is reproduced only within a moderate-rain regime rather than for arbitrary rain forcing.

4 Discussion

Our analysis shows that mesoscale vertical motions in the ~~trades strongly modulate~~ trade-wind regime modulate the marine boundary layer ~~moisture by counteracting~~ through a partial counteraction of entrainment-driven drying. Water vapor isotopologues reveal this ~~process with much~~ modulation with greater sensitivity than humidity alone, ~~highlighting~~ yielding an asymmetric response~~in which water vapor~~: δD ~~responds much more strongly to changes in mesoscale vertical velocities than~~ varies

Table 1. Parameter values used in the baseline drizzle model.

Quantity	Value	Basis
SST	27.3 °C	campaign mean
p	1013.25 hPa	surface pressure
h	700 m	campaign mean SCL depth
U	$8\ \mathrm{m\,s^{-1}}$	representative surface wind
C_E	1.2×10^{-3}	open-ocean bulk coefficient
q_{CL}	$13.0\ \mathrm{g\,kg^{-1}}$	dropsonde profiles
δD_{CL}	$-78‰$	dropsonde/isotope constraint
T_{cb}	18 °C	cloud-base temperature
δD_{oc}	$0‰$	VSMOW reference
P_{cb}	$5 \times 10^{-5}\ \mathrm{kg\,m^{-2}\,s^{-1}}$	weak trade-cumulus drizzle
χ	0.8	evaporated rain fraction
W_{width}	$4\ \mathrm{mm\,s^{-1}}$	W–rain transition scale
D/D' (surface flux)	1.0159	Merlivat and Jouzel (1979)
D/D' (rain evaporation)	1.024	Stewart (1975)
n	0.58	Stewart (1975)

more strongly with mesoscale vertical velocity than does the total mixing ratio. ~~A flux-form~~ The revised mixed-layer model ~~reproduces this behavior, demonstrating that δD responds about 7.5 times more strongly than humidity to mesoscale vertical motion. These findings underscore the critical role of mesoscale circulations in shaping humidity and isotopic composition in the trade-wind regime. Recall that throughout this study, E refers only to entrainment from the cloudy layer (CL) into the subcloud layer (SCL) and it does not include exchange between the CL and the free troposphere (FT)~~demonstrates one physically consistent mechanism for this asymmetry: below-cloud rain evaporation adds both vapor mass and isotopic mass, but for weak drizzle the added mass is small relative to the full moisture budget while the isotopic composition of the evaporated vapor is distinct from the ambient subcloud vapor.

~~Our findings can be placed in the context of the analytical and LES-based framework of Risi et al. (2020).In their simulations, the primary mechanism depleting near-surface vapor was the export of isotopically enriched air by convective updrafts, with downdrafts and rain evaporation providing additional contributions. They argued that the classical amount effect emerges because stronger large-scale ascent steepens vertical isotopic gradients, thereby enhancing the efficiency of updrafts and downdrafts in depleting the subcloud layer. In contrast, our EUREC^{4}A analysis highlights the sensitivity of~~

4.1 Model interpretation and constraints

Figure 8 provides the mechanistic closure for the observational regressions in Fig. 6. In the drizzle case, the model produces fitted δD ~~to mesoscale vertical motions within the trade inversion layer: shallow mesoscale updrafts counteract entrainment-driven~~

~~import of depleted~~ contours that are much more W-sensitive than the fitted humidity contours: $|\partial \delta D/\partial W|/|\partial \delta D/\partial E| = 1.66$, compared with $|\partial q/\partial W|/|\partial q/\partial E| = 0.44$ for humidity. This nearly fourfold contrast is the key quantitative result of the model. It shows that mesoscale ascent can strongly modify isotopic composition through W-dependent rain evaporation while leaving the total water vapor field primarily controlled by entrainment.

The no-rain control is equally important, but it should be interpreted within the structure of this process test. When $F_{\mathrm{rain}} = F_{\mathrm{rain},D} = 0$, both q and δD have nearly vertical fitted contours and zero W sensitivity because the model does not include direct W-driven vertical advection of the subcloud-layer budget. Surface evaporation plus cloudy-layer ~~air and thus enrich the subcloud layer, while mesoscale downdrafts enhance the isotopic depletion. Both perspectives underscore the role of vertical motions in setting near-surface isotopic composition, but at different scales and regimes: large-scale ascent and deep convection in Risi et al. (2020), versus shallow mesoscale overturning circulations within the trades in this study. Together, these results suggest that~~ entrainment therefore does not produce the observed non-parallel q–δD structure by itself in this model. Adding a third source term associated with below-cloud rain evaporation provides one physically plausible route to this structure. This does not mean that rain evaporation dominates the moisture budget; rather, the ~~isotopic composition of boundary layer vapor is highly sensitive to the scale and vertical structure of vertical motions, which can act either to enrich or to deplete depending on the dynamical context~~successful drizzle case occupies the regime in which rain evaporation is large enough to rotate the isotope contours but small enough that humidity remains E-dominated.

~~Our results provide mechanistic closure~~ This balance also constrains the interpretation. In sensitivity tests with much stronger precipitation forcing, the rain evaporation mass flux becomes large enough that q also rotates toward W sensitivity, and the q–δD contour separation collapses. The observed asymmetry is therefore not reproduced by arbitrary rain addition; it requires moderate below-cloud evaporation whose isotope effect is large relative to its net moisture effect. The model should consequently be viewed as an equilibrium process test rather than a unique retrieval of rain rate, rain intermittency, or microphysical parameters.

4.2 Connection to mesoscale overturning circulations and mixing–desiccation processes

These findings provide observational and mechanistic context for the shallow mesoscale overturning circulations (SMOCs) identified by George et al. (2023) and the counteraction mechanism proposed by Vogel et al. (2022). Vogel et al. (2022) ~~refuted the mixing-desiccation~~ demonstrated that mesoscale vertical motions counteract entrainment-driven drying, refuting the mixing–desiccation hypothesis of Sherwood et al. (2014) by showing that ~~mesoscale vertical motions and entrainment contribute comparably to subcloud-layer budgets, but with opposite signs for their impact on humidity. They concluded that~~ stronger mixing does not ~~desiccate cloud base because mesoscale circulations counteract the drying expected from entrainment. Meanwhile, George et al. (2023) provided the first~~ necessarily lead to cloud-base desiccation. George et al. (2023) provided direct observational evidence of SMOCs~~in the trade-wind layer, showing robust dipoles in divergence~~, documenting robust divergence dipoles between the subcloud and cloud layers ~~, spatial scales of $\sim$100–200 km, and ubiquitous coverage ($\sim 58\%$ of a $10^\circ \times 10^\circ$ domain). They demonstrated that SMOCs amplify moisture variance at cloud base, with strong anti-correlation between subcloud divergence anomalies and q at cloud base (Pearson $r \approx -0.67$), and proposed that~~ and showing that convergence branches reduce entrainment ~~drying efficiency in ascending regions, driving bottom-heavy moisture variance~~ efficiency and amplify moisture variance near cloud base.

~~By exploiting water vapor isotopologues, we bridge these complementary findings and provide a missing process-level attribution. Our δD measurements serve as direct tracers of source contributions, showing that mesoscale ascent maintains enriched isotopic signatures characteristic of oceanic evaporation, while entrainment introduces isotopically depleted air from the CL. This renders the qualitative compensation mechanisms of both studies directly observable in boundary-layer composition. Quantitatively, we show that mesoscale ascent offsets entrainment-driven depletion of δD with an efficiency of 1.19, meaning that 1 mm s^{-1} of upward motion more than cancels the isotopic effect of 1 mm s^{-1} of entrainment. For humidity, by contrast, the counteraction efficiency is only 0.30, thereby making the isotopic imprint a far more sensitive tracer of SMOC dynamics than humidity alone.~~

~~Our analysis extends both~~ Our analysis extends these studies by localizing the coupling mechanisms in the vertical. ~~We show that the~~ The strongest correlations between vertical velocity and both δD and humidity occur just below the subcloud layer top, ~~pinpointing~~ identifying where mesoscale circulations ~~leave their imprint on~~ most directly influence near-surface composition. This ~~vertical localization was not resolved in either previous study and sharpens the physical understanding of how SMOCs modulate the boundary layer . The isotopic approach also reveals that rising branches of SMOCs carry an ocean-evaporation signature into the subcloud and~~ height range is consistent with the layer where mesoscale vertical motion, cloud-base ~~layers, while descending branches are associated with entrained air from the CL, yielding enhanced δD contrast between branches that far~~ exchange, and evaporation of shallow precipitation are expected to interact most strongly. One plausible interpretation is that the $\sim$100 m offset of the δD correlation maximum below the SCL top marks the layer where mesoscale vertical motion samples condensate-derived vapor recently released by shallow precipitation evaporation near cloud base. We cannot separate this effect from the vertical structure of W alone with the present observations, but the combined observational and model evidence points to a three-flux balance among surface evaporation, cloudy-layer entrainment, and below-cloud rain evaporation. The resulting isotopic contrast between ascending and descending branches exceeds the corresponding ~~q~~ humidity contrast.

~~When scaled by their observed standard deviations,~~

4.3 Why isotopes respond more strongly than humidity

The pronounced isotopic sensitivity arises because δD responds ~~about 7.5 times more strongly to mesoscale vertical motion than does humidity , highlighting a novel asymmetry in the system's response to mesoscale variability. Small increases in entrainment lead to relatively large isotopic depletions with only modest drying. By mapping δD and q jointly onto the~~ to moisture source and phase-change history, whereas humidity is constrained by the total mass balance. Entrainment brings relatively dry, isotopically depleted cloudy-layer air into the subcloud layer. Surface evaporation supplies comparatively enriched vapor from the ocean. Below-cloud rain evaporation supplies a third contribution: condensate-derived vapor whose isotopic ratio reflects cloud-layer condensation followed by partial evaporation in unsaturated subcloud air. Mesoscale ascent can change the relative importance of these three fluxes in a way that strongly affects isotopic composition but only weakly alters total water vapor.

This asymmetry is evident in the joint entrainment–vertical velocity (E–W) space, ~~we demonstrate a diagonal organization very similar~~ where δD exhibits a strong diagonal organization analogous to the SMOC moisture anomaly structure described by George et al. (2023), but with ~~stronger isotopic amplitude, confirming and quantifying the proposed moisture-variance mechanism.~~

~~Our flux-form mixed-layer model provides mechanistic closure that bridges the conceptual frameworks of both studies. By parameterizing an effective entrainment frequency $\varepsilon_{\mathrm{eff}} \propto (E-\gamma W)$, the model captures the observed asymmetry between~~ larger amplitude. While both δD and ~~q without ad hoc tuning and reproduces the bottom-heavy variance patterns identified by George et al. (2023). This framework demonstrates that the greater sensitivity of isotopes arises naturally from the stronger contrast between δ values of surface and CL sources relative to their humidity differences.~~ humidity respond to entrainment, mesoscale ascent produces large isotopic enrichment with only modest moistening. Isotopic tracers therefore expose compensation mechanisms that remain largely hidden in humidity alone.

~~Thus, while our results broadly confirm the conclusions that mixing–desiccation fails in the trade-wind regime and that SMOCs fundamentally modulate boundary layer moisture, they advance our understanding by: (1) quantifying counteraction efficiencies, (2) providing source-specific attribution of moisture variability through isotopic tracers, (3) localizing the coupling mechanisms in the vertical, and (4) offering a simple yet physically grounded model framework. Together, these findings sharpen the refutation of the mixing–desiccation hypothesis, deepen our mechanistic understanding of SMOC-moisture coupling, and provide a pathway for incorporating isotope constraints into parameterizations of shallow convection and cloud feedbacks.~~

~~Our findings provide extensions to the theoretical frameworks for MBL water vapor isotopic compositionestablished by Benetti et al. (2018) and more recent empirical work by Galewsky et al. (2022) and Risi et al. (2019). While Benetti et al. (2018) demonstrated that their~~

4.4 Relation to existing isotope frameworks

Our results extend existing theoretical and observational frameworks for marine boundary layer isotopic composition. The MBL-mix ~~model successfully reproduces isotopic observations by incorporating both evaporative flux variability~~ framework of Benetti et al. (2018) successfully interprets isotopic variability through surface evaporation and mixing with isotopically depleted ~~free-tropospheric air , our study shows that mesoscale vertical velocities introduce an additional layer of complexity that fundamentally modulates these mixing processes. The counteraction efficiency we observe, where 1 mm s^{-1} of upward motion counteracts the isotopic effect of 1.19 mm s^{-1} of entrainment for δD, suggests that mesoscale circulations can completely overwhelm the traditional~~ air aloft. Our analysis indicates that active mesoscale periods include an additional rain-evaporation pathway, so the subcloud-layer isotope budget cannot always be reduced to a two-endmember ~~mixing framework during periods of strong vertical motion. This finding extends beyond the MBL-mix model's scope by demonstrating that the proportion of water vapor from the LFT (the r parameter in Benetti et al. (2018)) is not simply determined by entrainment rates but is dynamically modulated by mesoscale vertical velocities on timescales much shorter than typically considered.~~ balance between ocean evaporation and dry air aloft.

~~The asymmetric~~ Similarly, the asymmetric isotopic response we document ~~between δD and humidity to mesoscale forcing provides quantitative support for~~ is consistent with the processes outlined ~~in Galewsky et al. (2022), while revealing mechanisms that operate across different scales and environments. Our observations from EUREC4A show δD responding 7.5 times more strongly than humidity to mesoscale vertical motion (in σ-units), which parallels Galewsky et al. (2022)'s finding of stronger isotopic than humidity responses to decoupling in stratocumulus-topped boundary layers. However, our EUREC4A results~~ by Galewsky et al. (2022), who showed that water vapor isotopologues provide sensitivity to boundary layer mixing and decoupling processes in stratocumulus regimes that is not evident from humidity alone. Our EUREC^{4}A observations demonstrate that this ~~asymmetry~~ sensitivity extends to the trade cumulus regime and ~~operates on mesoscale rather than~~ is expressed through mesoscale overturning circulations rather than solely through boundary layer decoupling~~timescales~~. The vertical localization ~~we observe, with strongest correlations occurring just below the subcloud layer top, provides the missing~~ observed here provides a mechanistic link between ~~the~~ surface isotopic signatures and ~~the shallow mesoscale overturning circulations (SMOCs) identified by George et al. (2023). This suggests that the local sources of water vapor invoked by Galewsky et al. (2022) must be understood within the context of mesoscale~~ mesoscale circulation patterns that ~~can~~ transport locally evaporated ~~, but subsequently fractionated, water vapor between different levels of~~ but differentially processed vapor within the boundary layer.

Our ~~results further advance the understanding developed by Risi et al. (2019) regarding the relative importance of surface fluxes versus atmospheric mixing in controlling MBL isotopic composition. While Risi et al. (2019) demonstrated that boundary layer mixing processes could explain isotopic variability without invoking large-scale horizontal transport, our study reveals that the mixing itself is not a passive process but is actively modulated by mesoscale dynamics . The efficiency with which vertical velocity counteracts entrainment effects (efficiency $>$ 1.0 for δD) indicates that during periods of mesoscale ascent, the traditional closure assumptions fundamentally break down. The MBL cannot be treated as a simple~~ findings also complement the analysis of Risi et al. (2020), who emphasized the role of local mixing processes in controlling tropical surface-vapor isotopic variability. The EUREC^{4}A results indicate that active mesoscale periods cannot be represented as a simple two-endmember ~~system during active mesoscale periods, as the vertical motion effectively changes the isotopic composition of the entrained endmember by redistributing water vapor that has undergone different degrees of processing within the boundary layer. This finding reconciles the apparent contradiction between Risi et al. (2019)'s emphasis on local processes and the need to explain isotopic depletions that exceed what simple surface-atmosphere exchange can produce.~~ mixture between ocean evaporation and dry air aloft. A third, rain-evaporation source provides a physically plausible contribution because it changes isotopic composition without producing a proportional humidity anomaly.

4.5 Broader implications and limitations

The strong isotopic sensitivity to mesoscale vertical motion provides an observational constraint on boundary layer coupling that is not available from humidity alone. Large-eddy simulations have shown that shallow-cumulus organization can be coupled to mesoscale aggregation of moisture and convection (Bretherton and Blossey, 2017), and EUREC^{4}A observations show that observed moisture variance is strongly expressed near cloud base (George et al., 2023). Our isotopic observations demonstrate that mesoscale dynamics also leave a clear imprint on near-surface composition, indicating that δD is a sensitive tracer of mesoscale–surface coupling even when humidity anomalies are muted.

While our analysis focuses on mesoscale circulations, cold pools and precipitation also influence boundary layer structure during EUREC^{4}A (Touzé-Peiffer et al., 2022; Radtke et al., 2022). The strongest isotopic–vertical velocity correlations occur near 500–600 m, generally above the shallowest layers most strongly affected by cold-pool outflows. This suggests that the isotopic signal primarily reflects deeper mesoscale overturning and cloud-base exchange rather than only near-surface cold-pool dynamics, though future work explicitly incorporating cold-pool diagnostics and rain-rate observations would help further separate these influences. The synthetic equilibrium model is evaluated over $E = 10$–35 mm s^{-1}, so it is intended to diagnose the positive-entrainment regime that dominates the observational comparison, not the negative-E cases interpreted above as interface lowering or weak detrainment.

The ~~integration of our results with these previous studies reveals~~ W–rain relationship used in the model should not be interpreted as universal. It is likely to depend on cloud organization, aerosol conditions, precipitation efficiency, subcloud relative humidity, and the depth over which falling drops evaporate. These dependencies could change the strength of the isotope response in other trade-wind regimes or other forms of shallow convection. Likewise, the 60 h model integrations diagnose the equilibrium response to slowly varying forcing rather than the transient response to any individual 2 h observational sample. Because W enters the model only through the rain-activity function, the model cannot separate W-dependent precipitation effects from any direct vertical-advection effect of mesoscale motion on the SCL moisture budget. The more general result is that water isotopologues provide a sensitive constraint on whether mesoscale circulation changes moisture pathways mainly through entrainment, surface evaporation, rain evaporation, direct vertical advection, or some combination of these processes.

Overall, our results show that the marine boundary layer isotopic composition emerges from ~~a balance between surface evaporation(Craig–Gordon effects)~~the combined effects of surface evaporation, entrainment mixing~~(Benetti et al. (2018) framework), boundary layer decoupling processes (Galewsky et al. (2022) mechanisms)~~, below-cloud rain evaporation, and mesoscale circulation modulation~~(our new contribution). Rather than invalidating previous work, our study demonstrates that these assumptions hold only during quiescent periods and must be replaced by a more dynamic framework during periods of significant mesoscale activity. That mesoscale processes dominate over entrainment in determining surface isotopic signatures while showing weaker control over humiditysuggests that isotopic measurements provide a uniquely sensitive probe~~. These processes are not independent: mesoscale vertical motion changes the relative strength of each moisture pathway without producing proportional changes in humidity. This asymmetric response highlights the value of isotopic measurements as probes of mesoscale dynamics ~~that cannot be detected through humidity observations alone~~and provides a framework for incorporating isotope constraints into representations of shallow convection and cloud feedbacks.

5 Conclusions

The goal of this study was to quantify how mesoscale vertical motions modulate marine boundary layer moisture and isotopic composition in the ~~trade wind~~ trade-wind regime, and to test ~~the mixing–desiccation~~ interpretations of the mixing–desiccation hypothesis using water vapor isotopologue observations from EUREC^{4}A.

~~We found~~Our main findings are as follows:

1. Water vapor ~~δD responds approximately 7.5 times more strongly to~~ δD and mixing ratio exhibit distinct sensitivities to mesoscale circulation. While humidity variability is primarily controlled by entrainment, δD is more strongly modulated by mesoscale vertical velocity~~variations than humidity itself (when normalized by observed standard deviations), with δD showing a linear sensitivity of 3.72 $\sigma_{\delta D}$ per cm s^{-1} compared to 0.49 σ_q per cm s^{-1} for specific humidity~~, demonstrating that isotopic composition encodes mesoscale dynamics more clearly than humidity alone.

2. ~~Mesoscale upward motion counteracts entrainment-driven isotopic depletion with an efficiency of 1.19, meaning 1 mm s^{-1} of vertical velocity more than cancels the isotopic effect of 1 mm s^{-1} of entrainment, while the counteraction efficiency for humidity is only 0.30~~Using standardized regression coefficients, we find that mesoscale vertical velocity has a larger point-estimate counteraction efficiency for δD ($\eta_{\delta D} \approx 1.5$) than for humidity ($\eta_q \approx 0.25$). However, because these efficiencies are ratios of estimated coefficients and the confidence interval for $\eta_{\delta D}$ is broad, the data do not tightly constrain the magnitude of this contrast or rule out a smaller, statistically indistinct difference. We therefore interpret the efficiency contrast as suggestive rather than precisely resolved.

3. The strongest correlations between vertical velocity and both ~~δD~~ δD ($r \approx 0.52$) and mixing ratio ($r \approx 0.39$) occur within approximately ± 200 m of the subcloud layer top, ~~pinpointing~~ identifying the vertical region where mesoscale circulations ~~exert their primary influence on surface~~ most directly influence near-surface composition.

4. Periods of enhanced entrainment ~~consistently coincide~~ are consistently associated with more negative ~~δD~~ δD values and lower mixing ratios, ~~while~~ whereas periods of mesoscale ascent correspond to less negative ~~δD and higher humidity, demonstrating~~ δD and modest moistening. Together, these relationships reveal a systematic organization of boundary layer states across ~~the entrainment–vertical velocity parameter space~~entrainment–vertical velocity space, consistent with shallow mesoscale overturning circulations.

5. A steady-state, flux-form mixed-layer model with explicit below-cloud rain evaporation reproduces the observed asymmetric responses ~~, confirming that isotopic composition is more sensitive to changes in source mixing ratios than bulk humidity , thereby providing mechanistic~~ of δD and humidity. The drizzle case produces strong W sensitivity in δD while leaving humidity primarily E-dominated, whereas the no-rain control collapses the contour separation. This comparison identifies moderate, W-dependent rain evaporation as a mechanism that can provide closure for the ~~counteraction effects observed in the trade wind regime~~observed counteraction between entrainment and mesoscale ascent.

~~While the relatively small natural variability in δD~~ Although the natural variability of δD during the campaign ~~means that the precise~~ is modest and quantitative sensitivities should ~~be interpreted with caution~~therefore be interpreted cautiously, the convergence of ~~multiple diagnostics and agreement with the mechanistic model give confidence in the~~ observational diagnostics and model behavior supports a robust qualitative conclusion: ~~isotopic composition provides a far more~~ water vapor isotopologues provide a sensitive tracer of mesoscale circulations ~~than humidity alone.~~

6 ~~Flux-Form Mixed-Layer Model Formulation~~

5.1 ~~Model Overview~~

~~We use a steady-state~~in the trade-wind boundary layer that is not accessible from humidity measurements alone. These results refine interpretations of the mixing–desiccation hypothesis by showing that mesoscale vertical motions reorganize moisture pathways through a combination of entrainment, ~~flux-form mixed-layer model to represent the moisture and isotopic budgets of the subcloud layer (SCL) in the tropical marine boundary layer . The model is spatially homogeneous in the horizontal, has a fixed SCL height h, and resolves only bulk mean quantities: the specific humidity q_{BL} and the isotopic composition δ_{BL} of boundary-layer water vapor. The SCL exchanges water and isotopes with three reservoirs:~~

~~**Surface source:** evaporation from the ocean, with specific humidity q_{flux} and isotopic composition δ_{flux}. **Cloudy-Layer (CL) source:** entrainment of air from above the top of the SCL, with q_{FT}~~ surface evaporation, and ~~δ_{FT}. **Ventilation sink:** large-scale advection or lateral mixing at rate λ (s^{-1}).~~ below-cloud rain evaporation without producing commensurate changes in total water vapor, underscoring the value of isotopic constraints for understanding boundary layer dynamics and cloud–circulation coupling.

~~The model tracks the competition between these fluxes as modulated by the entrainment rate E and the mesoscale vertical velocity W. We introduce an "effective" entrainment frequency $\varepsilon_{\mathrm{eff}}$ to capture the modulation of entrainment by mesoscale motions .~~

Data availability. EUREC^{4}A water vapor isotope data from R/V Meteor and HALO/P3 dropsonde data from the JOANNE dataset are publicly available through the EUREC^{4}A data portal at https://eurec4a.eu/data.

5.1 ~~Governing Equations~~

~~Let q_{BL} be the boundary-layer specific humidity in g kg^{-1}, and R_{BL} the isotopic ratio (D/H) in absolute units. The steady-state moisture budget is~~

$$0 = \lambda\left(q_{\mathrm{flux}} - q_{\mathrm{BL}}\right) + \varepsilon_{\mathrm{eff}}\left(q_{\mathrm{FT}} - q_{\mathrm{BL}}\right),$$

~~where~~

$$\varepsilon_{\mathrm{eff}} = \max\left(\frac{E-\gamma W}{h}, 0\right).$$

~~Here E and W are in m s^{-1}, h in m, and γ is a dimensionless "counteraction efficiency" relating vertical velocity to effective entrainmentreduction. In the calculations presented here, $\gamma = 1.0$. Negative values of $\varepsilon_{\mathrm{eff}}$ are clipped to zero.~~

~~Solving (??) for q_{BL}:~~

$$q_{\mathrm{BL}} = \frac{q_{\mathrm{flux}}\,\lambda + q_{\mathrm{FT}}\,\varepsilon_{\mathrm{eff}}}{\lambda + \varepsilon_{\mathrm{eff}}}.$$

~~For the runs shown, q_{flux} is approximated by the saturation mixing ratio at the sea-surface temperature and pressure, $q_s(\mathrm{SST}, p)$, computed with the Tetens formula for $e_s(T)$ and~~

$$q_s = \frac{\varepsilon e_s}{p - e_s}, \quad \varepsilon = 0.622.$$

5.1 ~~Isotopic Balance~~

~~Let $R = 1 + \delta/1000$ be the conversion from δ notation (in ‰) to absolute isotopic ratio normalized to VSMOW. Denote R_{flux} and R_{FT} as the source isotopic ratios corresponding to δ_{flux} and δ_{FT}.~~

~~The steady-state isotopic mass balance is~~

$$0 = \lambda\,(q_{\mathrm{flux}}R_{\mathrm{flux}} - q_{\mathrm{BL}}R_{\mathrm{BL}}) + \varepsilon_{\mathrm{eff}}\,(q_{\mathrm{FT}}R_{\mathrm{FT}} - q_{\mathrm{BL}}R_{\mathrm{BL}})\,.$$

~~Solving for R_{BL}:~~

$$R_{\mathrm{BL}} = \frac{\lambda\,q_{\mathrm{flux}}R_{\mathrm{flux}} + \varepsilon_{\mathrm{eff}}\,q_{\mathrm{FT}}R_{\mathrm{FT}}}{(\lambda + \varepsilon_{\mathrm{eff}})\,q_{\mathrm{BL}}}.$$

~~The model output δ_{BL} is then~~

$$\delta_{\mathrm{BL}} = 1000\,(R_{\mathrm{BL}} - 1).$$

~~For the surface source isotopic composition δ_{flux}, the model by default uses the Craig–Gordon formulation, which depends on SST, relative humidity, and pressure. With the campaign-state values (SST = 27.3°C, RH = 0.716, $p = 101325$ Pa), this yields $\delta_{\mathrm{flux}} \approx -74.7$‰.~~

5.1 ~~Parameter Values Used~~

~~For the runs shown in the main text figures:~~

- ~~$h = 650$ m~~

- ~~$\gamma = 1.0$~~
- ~~$q_{\mathrm{FT}} = 3$ g kg^{-1}~~
- ~~$\delta_{\mathrm{FT}} = -150$ ‰~~
- ~~δ_{flux} from Craig–Gordon with SST = 27.3°C, RH = 0.716, $p = 101325$ Pa, giving ≈ -74.7 ‰~~
- ~~$\lambda = 0.10$ day^{-1} (converted to s^{-1} in computations)~~
- ~~E and W explored in ranges: $E \in [10, 35]$ mm s^{-1}, $W \in [-10, 10]$ mm s^{-1}~~

Author contributions. JG conceived the study, analyzed the data, developed the mixed-layer model, and wrote the manuscript. SL processed the isotopic data and contributed to the analysis. Both authors contributed to the interpretation and editing of the manuscript.

Competing interests. The authors declare no competing interests.

Acknowledgements. The authors used artificial intelligence (ChatGPT, OpenAI, 2025) to assist with coding the mixed-layer model and with drafting some initial text. All code, results, and manuscript content were thoroughly checked, validated, and revised by the authors, who take full responsibility for the accuracy and interpretation of the work. We acknowledge the ~~EUREC4A~~ EUREC^{4}A campaign organizers and participants, particularly the crew of R/V Meteor and the HALO and P3 aircraft operations team. This work was supported by the U.S. National Science Foundation under grant AGS-1853353. We thank the German Research Foundation (DFG) for support of the ~~EUREC4A~~ EUREC^{4}A campaign under grant 264907654.

References

Albright, A. L., Bony, S., Stevens, B., and Vogel, R.: Observed subcloud-layer moisture and heat budgets in the trades, Journal of the Atmospheric Sciences, 79, 2363–2385, https://doi.org/10.1175/JAS-D-21-0337.1, 2022.

Bailey, A., Aemisegger, F., Villiger, L., Los, S. A., Reverdin, G., Galewsky, J., Noone, D., and Steen-Larsen, H. C.: Isotopic measurements in water vapor, precipitation, and seawater during EUREC^{4}A, Earth System Science Data, 15, 465–495, https://doi.org/10.5194/essd-15-465-2023, 2023.

Benetti, M., Aloisi, G., Reverdin, G., Risi, C., and Sèze, G.: Importance of boundary layer mixing for the isotopic composition of surface vapor over the subtropical North Atlantic Ocean, Journal of Geophysical Research: Atmospheres, 123, 2442–2461, https://doi.org/10.1002/2017JD027593, 2018.

Bony, S. and Dufresne, J.-L.: Marine boundary layer clouds at the heart of tropical cloud feedback uncertainties in climate models, Geophysical Research Letters, 32, L20 806, https://doi.org/10.1029/2005GL023851, 2005.

Bony, S. and Stevens, B.: Measuring area-averaged vertical motions with dropsondes, Journal of the Atmospheric Sciences, 76, 767–783, https://doi.org/10.1175/JAS-D-18-0141.1, 2019.

Bony, S., Stevens, B., Ament, F., Albright, A., Acquistapace, C., Aemisegger, F., Farrell, D., Galewsky, J., Giez, A., Lenschow, D., Nuijens, L., Rauber, R., Röttenbacher, J., Schnitt, S., Schulz, H., Vial, J., Winker, D., and Zhang, L.: EUREC^{4}A: A field campaign to elucidate the couplings between clouds, convection and circulation, Surveys in Geophysics, 38, 1529–1568, https://doi.org/10.1007/s10712-017-9428-0, 2017.

Bretherton, C. S. and Blossey, P. N.: Understanding Mesoscale Aggregation of Shallow Cumulus Convection Using Large-Eddy Simulation, Journal of Advances in Modeling Earth Systems, 9, 2798–2821, https://doi.org/10.1002/2017MS000981, 2017.

Craig, H. and Gordon, L. I.: Deuterium and oxygen-18 variations in the ocean and the marine atmosphere, in: Stable Isotopes in Oceanographic Studies and Paleotemperatures, edited by Tongiorgi, E., pp. 9–130, Consiglio Nazionale delle Ricerche, Laboratorio di Geologia Nucleare, Pisa, Italy, 1965.

Galewsky, J., Steen-Larsen, H. C., Field, R. D., Worden, J., Risi, C., and Schneider, M.: Stable isotopes in atmospheric water vapor and applications to the hydrologic cycle, Reviews of Geophysics, 54, 809–865, https://doi.org/10.1002/2015RG000512, 2016.

Galewsky, J., Jensen, M. P., and Delp, J.: Marine Boundary Layer Decoupling and the Stable Isotopic Composition of Water Vapor, Journal of Geophysical Research: Atmospheres, 127, e2021JD035 470, https://doi.org/10.1029/2021JD035470, 2022.

George, G., Stevens, B., Bony, S., Pincus, R., Fairall, C., Schulz, H., Kölling, T., Kalen, Q. T., Klingebiel, M., Konow, H., Lundry, A., Prange, M., and Radtke, J.: JOANNE: Joint dropsonde observations of the atmosphere in tropical North Atlantic meso-scale environments, Earth System Science Data, 13, 5253–5272, https://doi.org/10.5194/essd-13-5253-2021, 2021.

George, G., Stevens, B., Bony, S., Vogel, R., and Naumann, A. K.: Widespread shallow mesoscale circulations observed in the trades, Nature Geoscience, 16, 584–589, https://doi.org/10.1038/s41561-023-01215-1, 2023.

~~Janssens, M., Vilà-Guerau de Arellano, J., van Heerwaarden, C. C., de Roode, S. R., Siebesma, A. P., and Glassmeier, F.: Nonprecipitating Shallow Cumulus Convection Is Intrinsically Unstable to Length Scale Growth, Journal of the Atmospheric Sciences, 80, 849–870, , 2023.~~

Graf, P., Wernli, H., Pfahl, S., and Sodemann, H.: A new interpretative framework for below-cloud effects on stable water isotopes in vapour and rain, Atmospheric Chemistry and Physics, 19, 747–765, https://doi.org/10.5194/acp-19-747-2019, 2019.

Konow, H., Ewald, F., George, G., Jacob, M., Klingebiel, M., Kölling, T., Luebke, A. E., Mieslinger, T., Pörtge, V., Radtke, J., Schäfer, M., Schulz, H., Vogel, R., Wirth, M., Bony, S., Crewell, S., Ehrlich, A., Forster, L., Giez, A., Gödde, F., Groß, S., Gutleben, M., Hagen, M., Hirsch, L., Jansen, F., Lang, T., Mayer, B., Mech, M., Prange, M., Schnitt, S., Vial, J., Walbröl, A., Wendisch, M., Wolf, K., Zinner, T., Zöger, M., Ament, F., and Stevens, B.: EUREC^{4}A's HALO, Earth System Science Data, 13, 5545–5563, https://doi.org/10.5194/essd-13-5545-2021, 2021.

Lenschow, D. H., Krummel, P. B., and Siems, S. T.: Measuring Entrainment, Divergence, and Vorticity on the Mesoscale from Aircraft, Journal of Atmospheric and Oceanic Technology, 16, 1384–1400, https://doi.org/10.1175/1520-0426(1999)016<1384:MEDAVO>2.0.CO;2, 1999.

Lenschow, D. H., Savic-Jovcic, V., and Stevens, B.: Divergence and vorticity from aircraft air motion measurements, Journal of Atmospheric and Oceanic Technology, 24, 2062–2072, https://doi.org/10.1175/2007JTECHA940.1, 2007.

Lilly, D. K.: Models of cloud-topped mixed layers under a strong inversion, Quarterly Journal of the Royal Meteorological Society, 94, 292–309, https://doi.org/10.1002/qj.49709440106, 1968.

Majoube, M.: Fractionnement en oxygène 18 et en deutérium entre l'eau et sa vapeur, Journal de Chimie Physique, 68, 1423–1436, https://doi.org/10.1051/jcp/1971681423, 1971.

Merlivat, L. and Jouzel, J.: Global climatic interpretation of the deuterium-oxygen 18 relationship for precipitation, Journal of Geophysical Research: Oceans, 84, 5029–5033, https://doi.org/10.1029/JC084iC08p05029, 1979.

Pincus, R., Fairall, C. W., Bailey, A., Chuang, P., de Boer, G., Doyle, J., Fuchs, D., Galewsky, J., Ghate, V., Greatbatch, R., Greenslade, C., Grise, K., Haines, S., Haynes, J. M., Heffernan, J., Isarra, A., Knuth, F., Lundry, A., Nester, A., Noone, D., Pfister, L., Quinn, P. K., Rajib, Z., Richard, E., Royer, H., Schulz, H., Sorooshian, A., Speingys, N., Spangler, C., Sullivan, S., Tjernström, M., Turnbull, J., Wang, H., Witte, M. K., and Zuidema, P.: Observations from the NOAA P-3 aircraft during ATOMIC, Earth System Science Data, 13, 3281–3296, https://doi.org/10.5194/essd-13-3281-2021, 2021.

Radtke, J., Naumann, A. K., Hagen, M., and Ament, F.: The relationship between precipitation and its spatial pattern in the trades observed during EUREC^{4}A, Quarterly Journal of the Royal Meteorological Society, 148, 1913–1928, https://doi.org/10.1002/qj.4284, 2022.

~~Risi, C., Hourdin, F., Cattiaux, J., Steen-Larsen, H. C., Wong, C. S., Galewsky, J., Lacour, J.-L., Bonne, J.-L., Clerbaux, C., Coheur, P.-F., Hurtmans, D., and Worden, J.: The water isotopic version of the LMDZgeneral circulation model, Atmospheric Chemistry and Physics, 19, 12 235–12 263, , 2019.~~

Risi, C., Muller, C., and Blossey, P. N.: What Controls the Water Vapor Isotopic Composition Near the Surface of Tropical Oceans? Results from an Analytical Model Constrained by Large-Eddy Simulations, Journal of Advances in Modeling Earth Systems, 12, e2020MS002 106, https://doi.org/10.1029/2020MS002106, 2020.

Sherwood, S. C., Bony, S., and Dufresne, J.-L.: Spread in model climate sensitivity traced to atmospheric convective mixing, Nature, 505, 37–42, https://doi.org/10.1038/nature12829, 2014.

Stevens, B., Bony, S., Farrell, D., Ament, F., Blyth, A., Fairall, C., Karstensen, J., Quinn, P. K., Speich, S., Acquistapace, C., Aemisegger, F., Albright, A. L., Bellenger, H., Bodenschatz, E., Caesar, K.-A., Chewitt-Lucas, R., de Boer, G., Delanoë, J., Denby, L., Ewald, F., Fildier, B., Forde, M., George, G., Gross, S., Hagen, M., Hausold, A., Heywood, K. J., Hirsch, L., Jacob, M., Jansen, F., Kinne, S., Klocke, D., Kölling, T., Konow, H., Lothon, M., Mohr, W., Naumann, A. K., Nuijens, L., Olivier, L., Pincus, R., Pöhlker, M., Reverdin, G., Roberts, G., Schnitt, S., Schulz, H., Siebesma, A. P., Stephan, C. C., Sullivan, P., Touzé-Peiffer, L., Vial, J., Vogel, R., Zuidema, P., Alexander, N., Alves, L., Arixi, S., Asmath, H., Bagheri, G., Baier, K., Bailey, A., Baranowski, D., Baron, A., Barrau, S., Barrett, P. A., Batier, F., Behrendt, A., Bendinger, A., Beucher, F., Bigorre, S., Blades, E., Blossey, P., Bock, O., Böing, S., Bosser, P., Bourras, D., Bouruet-

Aubertot, P., Bower, K., Branellec, P., Branger, H., Brennan, M., Brewer, A., Brilouet, P.-E., Brügmann, B., Buehler, S. A., Burke, E., Burton, R., Calmer, R., Canonici, J.-C., Carton, X., Cato Jr., G., Charles, J. A., Chazette, P., Chen, Y., Chilinski, M. T., Choularton, T., Chuang, P., Clarke, S., Coe, H., Cornet, C., Coutris, P., Couvreux, F., Crewell, S., Cronin, T., Cui, Z., Cuypers, Y., Daley, A., Damerell, G. M., Dauhut, T., Deneke, H., Desbios, J.-P., Dörner, S., Donner, S., Douet, V., Drushka, K., Dütsch, M., Ehrlich, A., Emanuel, K., Emmanouilidis, A., Etienne, J.-C., Etienne-Leblanc, S., Faure, G., Feingold, G., Ferrero, L., Fix, A., Flamant, C., Flatau, P. J., Foltz, G. R., Forster, L., Furtuna, I., Gadian, A., Galewsky, J., Gallagher, M., Gallimore, P., Gaston, C., Gentemann, C., Geyskens, N., Giez, A., Gollop, J., Gouirand, I., Gourbeyre, C., de Graaf, D., de Groot, G. E., Grosz, R., Güttler, J., Gutleben, M., Hall, K., Harris, G., Helfer, K. C., Henze, D., Herbert, C., Holanda, B., Ibanez-Landeta, A., Intrieri, J., Iyer, S., Julien, F., Kalesse, H., Kazil, J., Kellman, A., Kidane, A. T., Kirchner, U., Klingebiel, M., Körner, M., Kremper, L. A., Kretzschmar, J., Krüger, O., Kumala, W., Kurz, A., L'Hégaret, P., Labaste, M., Lachlan-Cope, T., Laing, A., Landschützer, P., Lang, T., Lange, D., Lange, I., Laplacette, C., Lavik, G., Laxenaire, R., Le Bihan, C., Leandro, M., Lefevre, N., Lena, M., Lenschow, D., Li, Q., Lloyd, G., Los, S., Losi, N., Lovell, O., Luneau, C., Makuch, P., Malinowski, S., Manta, G., Marinou, E., Marsden, N., Masson, S., Maury, N., Mayer, B., Mayers-Als, M., Mazel, C., McGeary, W., McWilliams, J. C., Mech, M., Mehlmann, M., Meroni, A. N., Mieslinger, T., Minikin, A., Minnett, P., Möller, G., Morfa Avalos, Y., Muller, C., Musat, I., Napoli, A., Neuberger, A., Noisel, C., Noone, D., Nordsiek, F., Nowak, J. L., Oswald, L., Parker, D. J., Peck, C., Person, R., Philippi, M., Plueddemann, A., Pöhlker, C., Pörtge, V., Pöschl, U., Pologne, L., Posyniak, M., Prange, M., Quiñones Meléndez, E., Radtke, J., Ramage, K., Reimann, J., Renault, L., Reus, K., Reyes, A., Ribbe, J., Ringel, M., Ritschel, M., Rocha, C. B., Rochetin, N., Röttenbacher, J., Rollo, C., Royer, H., Sadoulet, P., Saffin, L., Sandiford, S., Sandu, I., Schäfer, M., Schemann, V., Schirmacher, I., Schlenczek, O., Schmidt, J., Schröder, M., Schwarzenboeck, A., Sealy, A., Senff, C. J., Serikov, I., Shohan, S., Siddle, E., Smirnov, A., Späth, F., Spooner, B., Stolla, M. K., Szkółka, W., de Szoeke, S. P., Tarot, S., Tetoni, E., Thompson, E., Thomson, J., Tomassini, L., Totems, J., Ubele, A. A., Villiger, L., von Arx, J., Wagner, T., Walther, A., Webber, B., Wendisch, M., Whitehall, S., Wiltshire, A., Wing, A. A., Wirth, M., Wiskandt, J., Wolf, K., Worbes, L., Wright, E., Wulfmeyer, V., Young, S., Zhang, C., Zhang, D., Ziemen, F., Zinner, T., and Zöger, M.: EUREC^{4}A: An Atlantic trade-wind cloud experiment, Earth System Science Data, 13, 4067–4119, https://doi.org/10.5194/essd-13-4067-2021, 2021.

Stewart, M. K.: Stable isotope fractionation due to evaporation and isotopic exchange of falling waterdrops: Applications to atmospheric processes and evaporation of lakes, Journal of Geophysical Research, 80, 1133–1146, https://doi.org/10.1029/JC080i009p01133, 1975.

Stull, R. B.: The energetics of entrainment across a density interface, Journal of the Atmospheric Sciences, 33, 1260–1267, https://doi.org/10.1175/1520-0469(1976)033<1260:TEOEAD>2.0.CO;2, 1976.

Touzé-Peiffer, L., Vogel, R., and Rochetin, N.: Cold pools observed during EUREC^{4}A: detection and characterization from atmospheric soundings, Journal of Applied Meteorology and Climatology, 61, 593–610, https://doi.org/10.1175/JAMC-D-21-0048.1, 2022.

Tremoy, G., Vimeux, F., Soumana, I., Souley, I., Risi, C., Cattani, O., Favreau, G., and Oï, M.: Clustering mesoscale convective systems with laser-based water vapor δ^{18}O monitoring in Niamey (Niger), Journal of Geophysical Research: Atmospheres, 119, 5079–5103, https://doi.org/10.1002/2013JD020968, 2014.

Vogel, R., Albright, A. L., Vial, J., George, G., Stevens, B., and Bony, S.: Strong cloud–circulation coupling explains weak trade cumulus feedback, Nature, 612, 696–700, https://doi.org/10.1038/s41586-022-05364-y, 2022.